Diffusion coefficient estimations of radiometals in target solutions using microfluidic devices

A combined experimental & numerical study

B.S. Bekkema

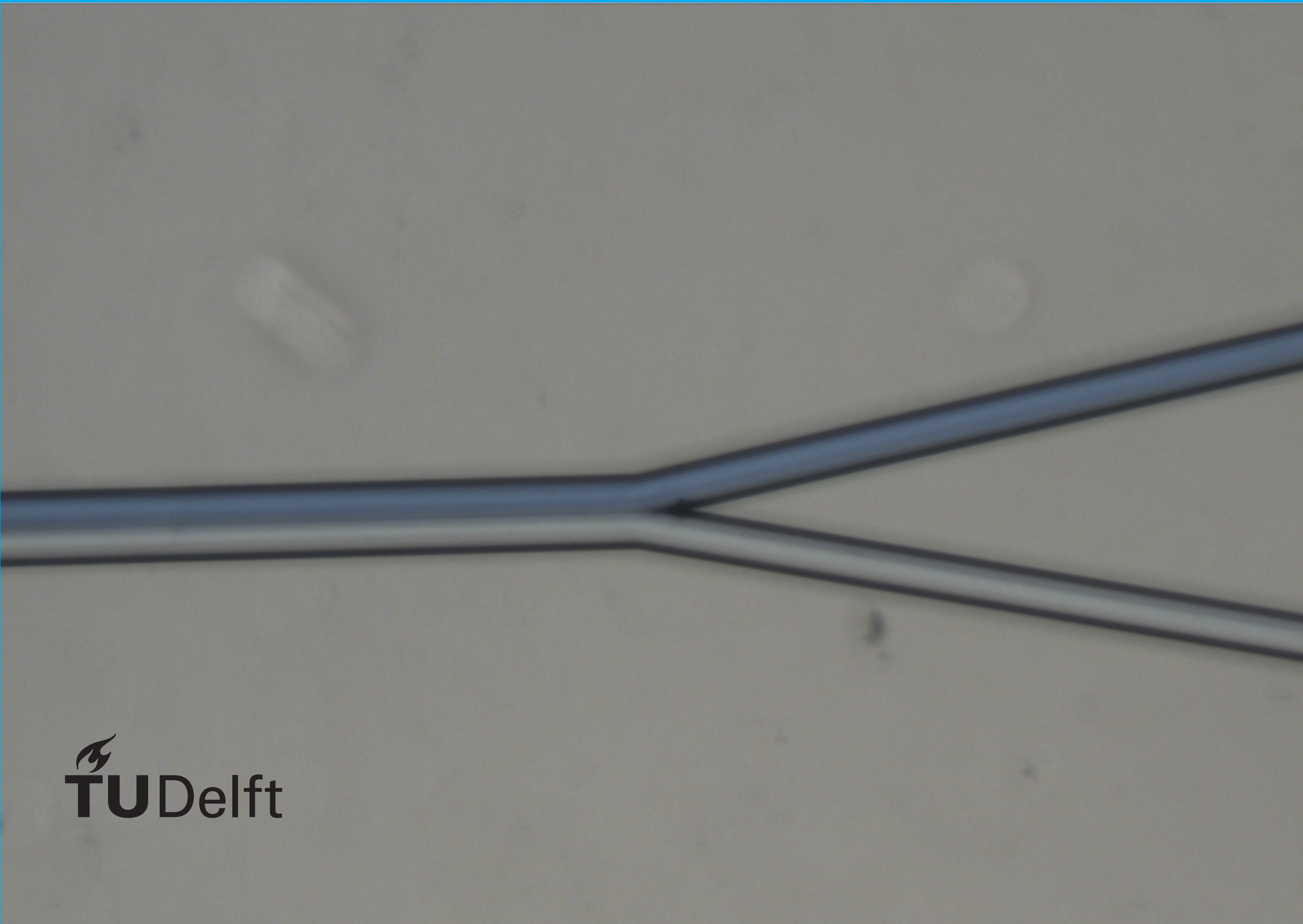

TU Delft

Diffusion coefficient estimations of radiometals in target solutions using microfluidic devices

A combined experimental & numerical study

by

B.S. Bekkema

to obtain the degree of Master of Science
at the Delft University of Technology,
to be defended publicly on Tuesday May 31, 2022 at 13:00 PM.

Student number:	5184274	
Project duration:	September 2021 – May, 2022	
Daily supervisors:	S. Trapp,	TU Delft
	A. Sudha,	TU Delft
Thesis committee:	Dr. ir. R. M. de Kruijff,	TU Delft, supervisor
	Dr. ir. M. Rohde,	TU Delft, supervisor
	Dr. ir. M. C. Goorden,	TU Delft

This thesis is confidential and cannot be made public until May 31, 2027.

Abstract

Radiometals re-emerge as a promising alternative in nuclear imaging. Cyclotron production of such radiometals using liquid targets solve critical impurity problems seen with current conventional production methods. Purification employing liquid-liquid extraction in microfluidic environments has recently been investigated. Fluid behaviour in microfluidic environments are deeply laminar, and one of the dominant factors in mass transfer in such environments is diffusion. For optimal design, numerical models are being developed to theoretically describe mass transfer in a microfluidic environment. To achieve this, diffusion coefficients of radiometals in their respective liquid target solutions need to be known. Exploiting the laminar flow properties in microfluidics, microfluidic devices have been employed in determining diffusion coefficients. This study presents a simplified 2D theoretical description of mass transfer in single phase flows in microfluidic channels. It has been attempted to verify the proposed model by determining the diffusion coefficient with methylene blue in an aqueous solution for direct comparison with literature. The method was tested for microfluidic devices of varying geometries, different flow rates and alternative setups, and yielded overestimations of a factor of two regarding literature. Consistently finding this overestimation, along with the discovery of several small mistakes in work presented in literature, does not render the method inaccurate. Further research in what range microfluidic devices remain an appropriate tool for determining diffusion coefficients is required. Diffusion coefficients for ^{68}Ga in target solutions of varying concentrations of zinc nitrate, dissolved in aqueous solutions of varying concentrations of nitric acid were investigated. The influence on concentration of nitric acid was minimal, while the diffusion coefficient was found to be inversely proportional to the viscosity of the target solution, in correspondence with the general behaviour of several empirical correlation relations for finding the diffusion coefficient.

B.S. Bekkema
Delft, May 2022

Nomenclature

Symbols & constants

ρ	Density	$[kg \cdot m^{-3}]$
t	Time	$[s]$
u	Velocity	$[m \cdot s^{-1}]$
p	Pressure	$[Pa]$
μ	Dynamic viscosity	$[Pa \cdot s, mPa \cdot s]$
ζ	Volume viscosity	$[Pa \cdot s]$
F	Force	$[N]$
L	Characteristic length scale	$[m]$
f	particle distribution function	[-]
x	position	$[m]$
ξ	microscopic particle velocity	$[m \cdot s^{-1}]$
Ω	Collision operator	[-]
τ	relaxation time	$[s]$
c_i	discrete velocity	$[m \cdot s-1]$
C	Concentration	$[mol \cdot L^{-1}, M]$
D	Diffusion coefficient	$[m^2 \cdot s-1, cm^2 \cdot s^{-1}]$
S_c	Source/sink term of concentration	$[mol \cdot L^{-1}, M]$
φ	General solution variable	[-]
k_b	Boltzmann constant	$1.38 \cdot 10^{-23}$ $[J \cdot K^{-1}]$
T	Temperature	$[K]$
r_h	Hydrodynamic radius	$[m]$
Φ_B	Association factor of solvent	[-]
M_B	Molecular weight of solvent	$[g \cdot mol^{-1}]$
V_A	molar volume of solute at its ebullition point	$[mL \cdot mol^{-1}]$
λ	Wavelength	$[nm]$
A	Absorbance	$[AU]$
I	light intensity	$[cd]$
ϵ	Extinction coefficient	$[M^{-1}cm^{-1}]$
d	Light path length	$[cm]$

Bold symbols indicate vectors.

List of Figures

List of Tables

Contents

1

Introduction

The use of radiometals re-emerges as a relevant alternative in molecular imaging and therapeutic applications, compared to biologically important isotopes such as ^{11}C, ^{13}N, and ^{15}O.[1,2] One of the earliest positron-emitting radionuclide to have been applied in clinical medicine, dating back to the 1960s[3], is ^{68}Ga, and has recently gained increased interest due to its expanding clinical applications.[4–6] Although ^{68}Ge/^{68}Ga generators were introduced over 50 years ago,[7] the recent growth of ^{68}Ga radiopharmaceuticals is due to immense progress in generator design. This newer generation of generators has solved critical impurity problems.[8,9] However, production rates are limited to performing elutions every four hours.[9,10] To provide a steady, continuous supply of ^{68}Ga, it can also be produced on a small to medium energy cyclotron via the ^{68}Zn(p,n)^{68}Ga reaction. The direct cyclotron production of ^{68}Ga is based on the proton irradiation of enriched ^{68}Zn, as either a solid or a solution target.[11,12] Next, one must chemically process the irradiated ^{68}Ga/^{68}Zn target to remove the bulk zinc and other metal contaminants prior to radiolabelling.[13] Conventional methods for the purification of ^{68}Ga isotopes such as ion exchange resin columns are slow processes, which hurt the production of ^{68}Ga due to its relatively short half life of 67.8 minutes.[14] A promising alternative aims to circumvent such inconveniences through microfluidic solvent extraction.

Solvent extraction is a separation process of chemical compounds based on differences in their solubility in two immiscible fluids.[15–18] Most metal ions are not soluble in organic liquids by themselves, but by adding a chelating agent, metal compounds can be selectively dissolved.[19] Industrial forms of solvent extraction rely on mixer-settlers, centrifugal contactors and columns.[20–22] Such machines utilise large amounts of hazardous solvents and usually require long settling times.[23] Reducing the dimensions of the geometry to the microscale in which solvent extraction is performed, gives rise to several advantages, including a higher surface-to-volume ratio and subsequently shorter diffusion lengths. This leads to an increased extraction efficiency, even at extremely low concentrations.[24,25] Figure 1.1 provides a schematic overview of the microfluidic extraction process.

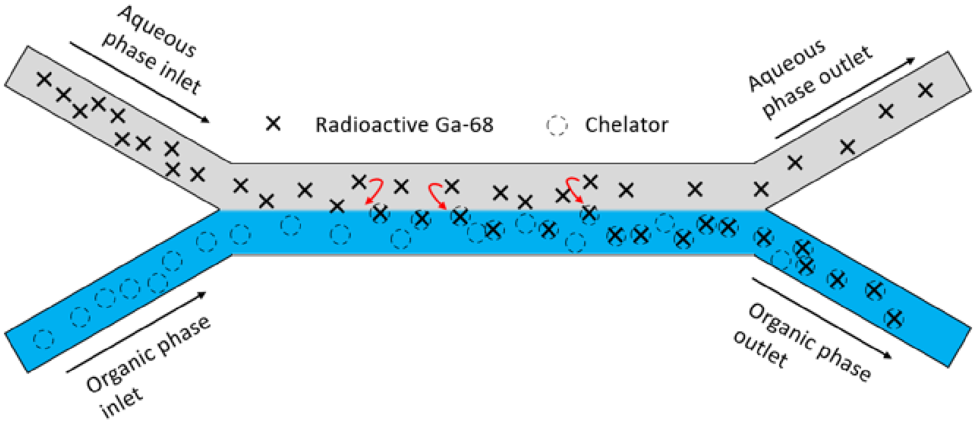

Figure 1.1: A schematic overview of the extraction mechanism of ^{68}Ga isotopes in a microfluidic channel.

To accurately predict extraction efficiencies, one needs a thorough theoretical description of the physical processes inside the microfluidic channel. One of these processes is the random individual molecular motion of the solute to the fluid-fluid interface inside the microchannel, which manifests itself on the macroscale as *diffusion*,[26,27] allowing it to be captured by the chelating agent. The knowledge of the diffusion coefficient is crucial to describe the fate of a diffusing substance and all the diffusion-related phenomena. For spherical objects, the value of the diffusion coefficient can be theoretically derived from the Stokes–Einstein relation.[28] Other conventional methods for determining diffusion coefficients in liquids, which are typically based on monitoring macroscopic concentration gradients include the diaphragm cell,[29] Taylor dispersion,[30] dynamic light scattering,[31] and Fluorescent correlation spectroscopy.[32] Drawbacks to these methods include they are based on indirect measurements, require large sample volumes or require costly and complicated instrumentation. Recently, aside from their use in isotope purification, microfluidic devices have emerged as promising alternative to overcome such limitations for the determination of diffusion coefficients.[33–38] These methods rely on the laminar flow properties of fluids residing in microfluidic channels, such that transversal mass transfer occurs solely by diffusion. By having two co-flowing streams, one containing a selected solute in a selected solvent, while the other is pure solvent, observations on the amount of solute transferred can reveal diffusion properties.[35]. This is achieved by providing a theoretical description of fluid flow and mass transfer in a microfluidic environment, from which the amount of transferred solute can be numerically calculated. Comparing these calculations with experimental results, lead to an estimate of the diffusion coefficient of the selected solute in its respective solvent. Previous work by Miložič *et al.* has claimed this method to be accurate for methylene blue in water to within 5% when compared to empirical relations, such as Stokes-Einstein,[28] Wilke-Chang and Siddiqi-Lucas,[39,40]. Häusler *et al*. proved the method to be accurate for various electrolytes in infinite dilution to within 1%. Their methods involve a 3D numerical description of the diffusion process in microfluidic channels, and are not descriptive in how they extract relevant data from their developed numerical models. This study proposes a simplified 2D description of mass transfer in microfluidic channels, and aims to verify whether microfluidic devices are an appropriate tool for estimation diffusion coefficients. Furthermore, the diffusion coefficient of ^{68}Ga is determined in various liquid target solutions.

1.1. Thesis outline

This project aims to estimate diffusion coefficients of ^{68}Ga in an aqueous solution of zinc nitrate, specifically.[11] This leads to the following research questions:

- What are the diffusion coefficients of ^{68}Ga in various liquid target solutions?
- Can microfluidic channels be successfully applied for estimating diffusion coefficients?
    - Is a 2D description of the physical process in a microfluidic environment sufficient for accurate diffusion coefficient estimation?

This study will provide sufficient theoretical knowledge for fully understanding its concepts, after which a thorough description of experimental methods is provided, along with an overview of the results and a brief conclusion.

2

Theory

This chapter shortly describes all necessary knowledge to fully understand the concepts of this study. It briefly reviews certain branches of production methods for radioisotopes used in medicine today, and explains general concepts encountered in (numerical) fluid mechanics. This allows for an adequate description of purification steps as part of previously mentioned production methods.

2.1. Nuclear Medicine & PET

Nuclear medicine exploits the unique characteristics radioactive elements possess, such as the emission of particles or electromagnetic radiation, to diagnose and treat a plethora of diseases.[41,42] Commonly used imaging techniques for diagnosis of most types of cancer and tumours are Single-Photon Emission Computed Tomography (SPECT) and Positron Emission Tomography (PET). An increase in interest in the use of radiometals has been developed over the recent years, as their wide range of decay characteristics, such as half-life, decay energy, decay mode and branching ratios, enable unsurpassed specificity for selecting therapeutic or diagnostic techniques.[43–45] PET is an imaging technique where a patient is administered a radioisotope that emits β^+-radiation. When this positron finds one of the abundant electrons in the human body, it annihilates into two 511 keV γ-rays, emitted in opposite directions.[46,47] The patient is surrounded by a ring of detectors, as illustrated in Fig. 2.1. These annihilation photons are registered by detectors on opposite sides of the ring, only when two detectors each detect a photon simultaneously, i.e., within 10 to 25 ns of each other. This allows the position of origin to be deduced from their relative intensities. From sufficient amounts of such data points the activity distribution within the plane of detection can be reconstructed, providing an image of any cancerous growth.[46]

2.2. Production of gallium-68

Common methods of isotope production include target irradiation in a nuclear reactor with neutrons, and charged particle irradiation, which can be accelerated by either a linear accelerator or cyclotron[46,48]. Cyclotron targets can be irradiated while residing in three common states of matter: solid, liquid and gas. Isotopes with a low atomic weight, such as ^{11}C or ^{18}F, are preferably produced with a gaseous or liquid target. Medium to high atomic weight isotopes, particularly metals, are produced with a solid target.[43] For the production of large activities, a higher beam current and higher target densities are required, thus the use of solid targets is the preferred option. Solid target irradiation does have several drawbacks, as it is a costly endeavor, has tremendous operational complexity, and poses difficulties during post-irradiation handling and transport compared to gaseous and liquid target irradiation.[43] Biomedical cyclotrons, commonly found in hospitals and universities, generally operate at low beam energies (< 20 MeV). These are perfectly capable of producing aforementioned low atomic weight isotopes, and recently it has also been shown by the International Atomic Energy Agency that they are certainly adequate for the production of radiometals in liquid targets, ^{68}Ga among them.[49]

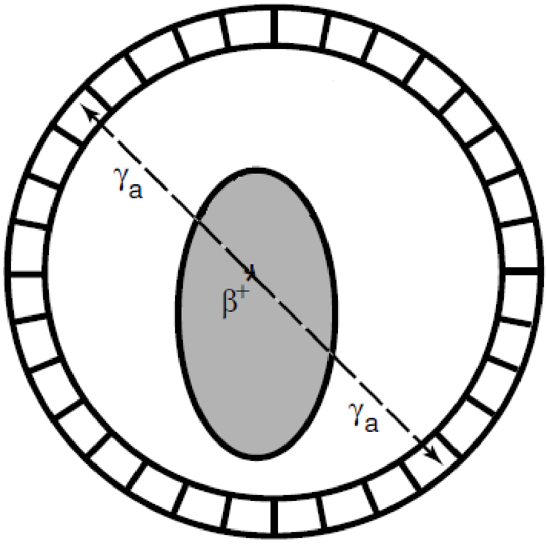

Figure 2.1: PET imaging of an object surrounded by a ring of detectors.[46]

2.2.1. Liquid Isotope Production

The production of radiometals in liquid targets is based on the dissolution of the target material in a strong acid and then diluting the resulting metal-salt in acid solution (typically in 0.01 to 1 M range) for loading into the liquid target. Jensen *et al.* demonstrated the production of ~2 GBq ^{68}Ga in an aqueous enriched [^{68}Zn]ZnCl$_2$.[50] The first successful ^{68}Ga production in a liquid target using enriched ^{68}Zn nitrate in dilute nitric acid was reported by Pandey *et al.* in 2014.[11] This was followed up shortly by other authors.[51–53] Salt-based target solutions inevitably present lower densities of target material, and thus lower production yields when compared to the corresponding solid targets. Recent results demonstrate that the technique provides adequate activities for clinical use on a daily basis, however, with improved convenience because reduced post-irradiation processing (and associated decay) partially compensates for the lower activity levels produced. It provides a convenient alternative to the conventional ^{68}Ge/^{68}Ga generators for the routine production of ^{68}Ga.[11]

2.3. Fluid dynamics

Typically, the field of fluid dynamics concerns itself with the macroscopic motion of fluids and gases. This implies that the fluid concept can be considered a continuum one. When describing a fluid element, such a volume contains many molecules. This fluid element is small with respect to the system size, but large in comparison to the size of each individual molecule and the average distance between them.[54,55]

It typically starts out by a generalisation of the conservation of mass in the form of a partial differential equation (PDE) known as the *continuity equation*:

$$\frac{\partial \rho}{\partial t} + \nabla \cdot (\rho \mathbf{u}) = 0 \tag{2.1}$$

where ρ is the density, t the time, and $\mathbf{u}$ the velocity.

Similarly, the conservation of momentum can also be mathematically generalised with the *Navier-Stokes equation*:

$$\rho\left(\underbrace{\frac{\partial \mathbf{u}}{\partial t}}_{\text{Transient}} + \underbrace{\mathbf{u}\cdot\nabla\mathbf{u}}_{\text{Convection}}\right) = \underbrace{-\nabla p}_{\text{Pressure}} + \underbrace{\nabla\cdot\left\{\mu\left(\nabla\mathbf{u} + \nabla(\nabla\cdot\mathbf{u}) - \frac{2}{3}(\nabla\cdot\mathbf{u})\mathbf{I}\right) + \zeta(\nabla\cdot\mathbf{u})\mathbf{I}\right\}}_{\text{Viscous stress tensor}} + \underbrace{\mathbf{F}}_{\text{Ext. forces}} \tag{2.2}$$

where p is pressure, μ is the dynamic viscosity and ζ the second or volume viscosity, and **F** represents any type of external force acting on the fluid, such as gravity or an electric field. This equation is generally difficult to solve, but for some specific situations with certain assumptions, the equation simplifies tremendously.[55] For liquids, which are generally incompressible, the continuity equation (2.1) simplifies to:

$$\nabla \cdot \mathbf{u} = 0 \tag{2.3}$$

When substituting equation 2.3 into equation 2.2 it is easy to see that this allows for the Navier-Stokes Equations to be written in its most common form:

$$\rho \frac{\partial \mathbf{u}}{\partial t} + \mathbf{u} \cdot \nabla \mathbf{u} = -\nabla p + \mu \Delta \mathbf{u} + \mathbf{F} \tag{2.4}$$

Even for this much simpler form, analytical solutions are only available for fairly simple cases, such as the Couette or Poiseuille flows in two dimensions, as the non-linear convection term naturally vanishes.[56,57] Most cases involve more complex geometries and boundary conditions and largely need to be solved using numerical methods.

2.3.1. Microfluidics

An important number in the study of fluid behaviour is the Reynolds number. This number represent the ratio of inertial and viscous forces and is given by:

$$Re = \frac{\rho u L}{\mu} \tag{2.5}$$

where ρ is the density in $kg \cdot m^{-3}$, u the velocity in $m\ s^{-1}$, L the characteristic length scale, and μ the dynamic viscosity in $Pa \cdot s$.

Reynolds numbers for fluids in a microfluidic environment can be estimated as follows; water with an assumed constant density flows with a typical velocity in a range of $\mu m\ s^{-1}$ - $cm\ s^{-1}$ in typical channel radii in a range of 1-100 μm,[58] yields a range of Reynolds numbers in the order of $\mathcal{O}(10^{-6})$ to $\mathcal{O}(10)$.[59] Such low Reynolds numbers indicate that viscous forces are dominant in microfluidic systems, and the flow can be regarded as laminar.[55] When inertial forces are small compared to viscous forces, which is usually the case in microfluidic environments, the nonlinear term in 2.4 can be neglected.[59] When assumed fluid flow has fully developed and no external forces are acting on the system, the transient and force terms can also be neglected. This reduces equation 2.4 to:

$$\nabla p = \mu \Delta \mathbf{u} \tag{2.6}$$

For the laminar properties of fluids in a microfluidic environment, microfluidic devices are promising instruments for the purification of radioisotopes, by means of fluid-fluid extraction.[60,61] After production of the radioisotope in its target solution, it requires chemical separation before operational use, for which microfluidic devices possess several advantageous properties compared to their macro counter parts: a high surface to volume ratio; only a small amount of sample is required; handling of liquids that are difficult to handle with traditional technologies; and the most relevant for this research; low Reynolds number flow (i.e. laminar flow), resulting in mass transfer in the microchannel solely in the form of streamwise convection and spanwise diffusion.[15,58]

2.4. Computational fluid dynamics

Powerful methods for approximating solutions to the incompressible Navier-Stokes equations reside in computational fluid dynamics (CFD). CFD utilises a discretisation method to approximate the governing PDEs by a system of algebraic equations, which can be solved numerically.[62] These approximations are applied to small domains in time and space, such that the numerical solution only exists at these discrete nodes. For processes which are well understood, i.e., the governing equations are known accurately, solutions of any order of accuracy can be achieved,[63] making CFD one of the most widely used methods for solving fluid flows today. Commonly employed methods in the continuum assumption are finite difference methods, where derivatives are approximated by Taylor-expansion around each node in discretised space and time, and is broadly used for its simplicity.[64] Finite volume methods share many similarities with finite difference methods, but can be employed to solve the equation on more complex geometries by discretising the simulation domain into irregular grids.[65] Other approaches in solving the equations of fluid dynamics, is by regarding the fluid as a collection of particles. Such particles can represent anything from singular atoms, molecules, or collections of molecules. Methods where single atoms are tracked, usually require large amounts of computational effort to describe fluids at the macro level, and are prone to statistical noise. Lattice Boltzmann methods solved the problem of this statistical noise by providing a mesoscopic description of fluid behaviour.[66] In macroscopic methods, much of the complexity in solving the equations in fluid mechanics, arises from approximating derivatives found in the non-linear convection term.[67] The kinetic nature of the lattice Boltzmann method allows for a linear description of the convection term. Interactions between nodes are entirely linear, while the method introduces non-linearity in a local collision process on each discrete node. Such local properties also allows for the model to be easily extended to multi-phase flow,[68] which is attractive for describing solvent extraction in microfluidic channels assisted by chelation, making lattice Boltzmann methods the suitable choice for solving for the fluid flow in microfluidic channels. The methods employed in this study are further explored in the following sections.

2.4.1. Lattice Boltzmann

Lattice Boltzmann methods are derived from kinetic theory.[69] Kinetic theory describes fluid motion of dilute gases at the mesoscopic scale, meaning fluid elements are described by distributions of particles. The premise of lattice Boltzmann methods is to the construct a simplified kinetic model that encompasses the underlying physics of microscopic and/or mesoscopic mechanisms such that the macroscopic averaged properties obey the relevant macroscopic equations.[67] The main argument for using these simplified kinetic-type methods for macroscopic fluid flows stems from the fact that macroscopic behaviour of fluid flow emerges from the collective behaviour of microscopic particles, even when omitting underlying details.[70] The fundamental variable in kinetic theory is the particle distribution function, which is a probabilistic distribution of a group of particles, typically annotated as $f(\mathbf{x}, \boldsymbol{\xi}, t)$. It should be regarded as a generalisation of the density ρ at position $\mathbf{x}$. It also keeps track of the microscopic particle velocity $\boldsymbol{\xi}$. From this particle distribution function, macroscopic quantities such as the physical density ρ and momentum density $\rho\mathbf{u}$ can be extracted as follows:[71]

$$\rho(\mathbf{x}, t) = \int f(\mathbf{x}, \boldsymbol{\xi}, t) d^3\xi \tag{2.7}$$

$$\rho(\mathbf{x}, t)\mathbf{u} = \int \boldsymbol{\xi} f(\mathbf{x}, \boldsymbol{\xi}, t) d^3\xi \tag{2.8}$$

The evolution of the particle distribution function in time can be found by taking its derivative with respect to time, leading directly to the Boltzmann equation:

$$\frac{\partial f}{\partial t} + \boldsymbol{\xi}\frac{\partial f}{\partial \mathbf{x}} + \frac{\mathbf{F}}{\rho}\frac{\partial f}{\partial \boldsymbol{\xi}} = \Omega(f) \tag{2.9}$$

The right-hand side of this equation represents a source term in the form of a the so-called *collision operator*. Boltzmann's original collision operator is of the form of a complicated and cumbersome double integral over velocity space. It considers all the possible outcomes of two-particle collisions for any choice of intermolecular forces. A more simplistic approach is proposed by Bhatnagar, Gross and Krook, who outlined the operator as a relaxation towards a local equilibrium, based on the assumption that molecular interactions tend to even out the angular distribution of particle velocities around the mean velocity.[72] This operator is given by 2.10

$$\Omega(f) = -\frac{(f - f^{\mathrm{eq}})}{\tau} \tag{2.10}$$

where τ, known as the *relaxation time*, represents the speed at which the system equilibrates. This parameter τ directly correlates to physical properties such as viscosity and heat diffusivity of the fluid.

Now that a formulation of the Boltzmann equation is established, an approach on solving this equation is needed. Solving the Boltzmann equation analytically is typically even harder than for the Navier-Stokes equations, but numerical approximations to the Boltzmann equation can paradoxically be obtained with relative ease.[71] The first step for solving the equation numerically is by discretising physical space, time and velocity space. The discrete counterpart of the Boltzmann equation is often referred to as *lattice Boltzmann equation* and is given by:

$$f_i\left(\mathbf{x}+\mathbf{c}_i\Delta t, t+\Delta t\right) = f_i(\mathbf{x},t) + \Omega_i(\mathbf{x},t) \tag{2.11}$$

where the subscript i stands for the *i*th velocity component of the discrete particle distribution f at position x at time t. The equation describes how f_i moves with velocity $\mathbf{c}_i$ to a neighbouring node $\mathbf{x}+\mathbf{c}_i\Delta t$ at the next time step $t+\Delta t$. Discretising velocity space is done by choosing a certain velocity set, containing the discrete velocities and their respective weighting coefficients. The shape and size of these velocity sets based on the dimensionality of the problem, and the trade-off between computational effort and accuracy.[73] Some of the most widely used velocity sets in 2D are shown in fig. 2.2.

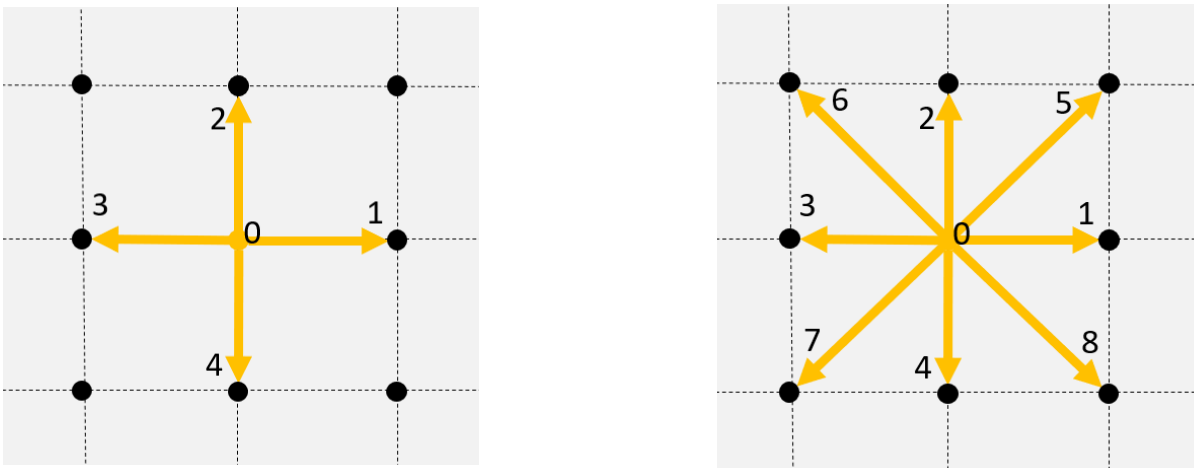

(a) D2Q5 velocity set

(b) D2Q9 velocity set

Figure 2.2: Discrete velocity sets in 2D

To briefly summarise, the Lattice Boltzmann method finds a numerical solution to the Boltzmann equation by simulating distributions of particles, discrete distribution functions, at different nodes (lattice points) in space. The flow of the fluid is simulated through the collision of said particle distributions and streaming towards neighbouring nodes, as illustrated in fig. 2.3. This process is repeated for every timestep until the solution has converged to its desired accuracy.[68]

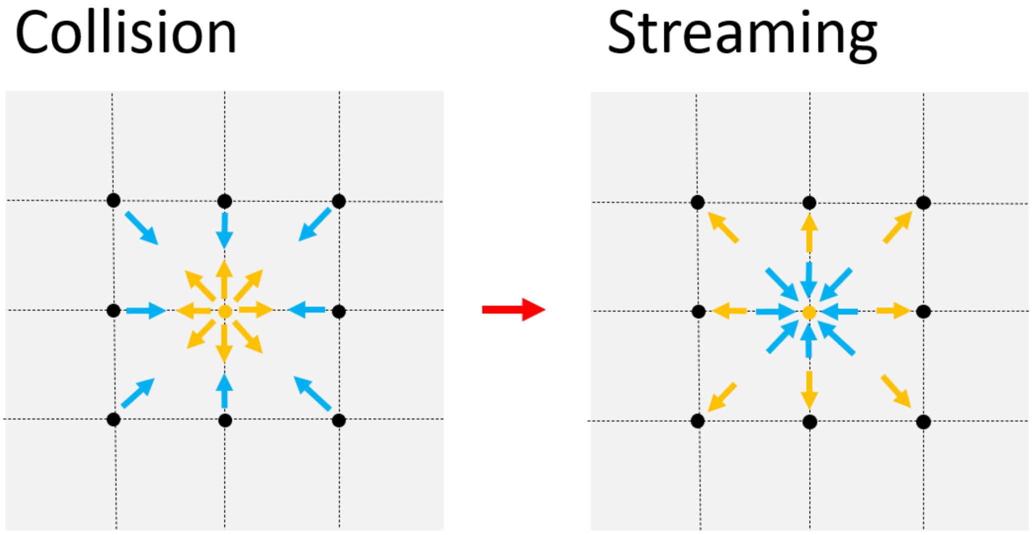

Figure 2.3: A schematic overview of how particle distribution function is discretised in physical and velocity space.

The discretised lattice Boltzmann equation leads directly to the equations of fluid dynamics on the macroscale, as can be shown per the Chapman-Enskog Analysis.[74] Therefore, from a solution of the Boltzmann equation for a given case the solution to the Navier-Stokes Equations for the same case can often be found.

2.5. Mass transport mechanisms and computational methods

The fluxes of energy, momentum and mass each have two main modes of transport; transport by convection, which accompanies any bulk motion, and diffusive transport, which is attributed to small-scale molecular displacements.[75] As with fluid dynamics, the motion of mass can be described with a general formulation of a conservation principle. Inspection of the governing equations of various physical phenomena will conclude that the conservation of a chemical species C is described by:[76]

$$\underbrace{\frac{\partial \rho C}{\partial t}}_{\text{Transient term}} + \underbrace{\nabla \cdot (\rho \mathbf{u} C)}_{\text{Convection term}} = \underbrace{\nabla \cdot (D \nabla C)}_{\text{Diffusion term}} + \underbrace{S_C}_{\text{Source term}} \tag{2.12}$$

Where the transient term described the evolution of the concentration C in time, the convective term describes the rate of change in C due to bulk motion, the diffusive term accounts for molecular transport of the species C and the source term describes any creation/destruction of the species.

An important dimensionless number in the study of mass transport is the Péclet number.[77] This number expresses the ratio between convective and diffusive mass transport and can be used to determine whether diffusive of convective mass transport is dominant in a given system. It is defined as:

$$Pe = \frac{uL}{D} \tag{2.13}$$

where L represents the characteristic length alongside the direction of flow, u the flow velocity and D the diffusion coefficient.

Similar to solving the Navier-Stokes equations, solving equation 2.12 is generally quite complex, and it is routinely approximated by numerical methods based on CFD models.[76] The following section describes one of the most widely used methods for numerically solving equation 2.12, due to its simplicity, stability and short computation times.[78]

2.5.1. Finite difference

The finite difference method discretises physical space into a grid of nodes. On these nodes, the solution variables are represented by just a value associated with each node, e.g., a general solution variable $\varphi(x_i)$. This solution variable is approximated by its discrete counterpart $\varphi_i(x_i)$. These approximations are based on the local Taylor expansion of the solution variable from which an expression for any arbitrary order derivatives of φ can be obtained.[77] The most straightforward example of this is approximating the first order derivative of φ as:

$$\frac{d\varphi_i}{dx} = \frac{\varphi_i(x_{i+1}) - \varphi_i(x_i)}{\Delta x} \tag{2.14}$$

which is commonly called the first order *forward* difference of first order accuracy, as it determines the rate of change of the variable φ_i when looking at the forward node. A similar approach yields an expression for the first order *backward* difference:

$$\frac{d\varphi_i}{dx} = \frac{\varphi_i(x_i) - \varphi_i(x_{i-1})}{\Delta x} \tag{2.15}$$

Both these approximations have truncation errors which scale with Δx, meaning that when the grid of nodes is refined, the error scales linearly with said refinement. Another finite difference approach to the first order derivative is the central difference scheme, which implements the rate of change as function of both directions :

$$\frac{d\varphi_i}{dx} = \frac{\varphi_i(x_{i+1}) - \varphi_i(x_{i-1})}{2\Delta x} \tag{2.16}$$

The central difference approximation truncation error scales with Δx^2, meaning this approximation is *second* order accurate. In this case the error decreases rapidly with increasing mesh resolutions. All three of these approximations can be extended to describe derivatives of any integer order, to the desired level of accuracy. This method is simple in practice, although some care should be taken as how to convert the derivatives into their appropriate finite difference counterparts, e.g., when a fluid experiences strong convection in the positive x-direction, all the information the fluid carries comes in from the left. Therefore, in such cases, a backward difference approximation is much more favourable. Small variations in this method include the distinction between explicit and implicit methods. Explicit methods compute the solution at the current timestep which explicitly depends on the solution of previous timesteps, for which stability criteria need to be taken into account. Implicit methods, where the solution on the current timestep is recursively dependent on values at the current timestep, are less concerned with stability issues.[79]

2.6. Diffusion coefficient estimation

2.6.1. Empirical correlation relations

Stokes- Einstein
The Stokes-Einstein equation specifically applies to a solute consisting of spherical particles, and is valid typically when these spherical molecules are dissolved in a solvent consisting of smaller size compared to the solute.[80] Many empirical correlation relations for estimating liquid phase diffusion coefficients have been derived from it. It is given by:

$$D = \frac{k_b T}{6\pi\mu r_h} \tag{2.17}$$

Where D is the diffusion coefficient in $m^2 s^{-1}$, k_b the Boltzmann constant, T the temperature in K, μ the dynamic viscosity in $Pa \cdot s$ and r_h the hydrodynamic radius of the solute in m.

Wilke-Chang Correlation
The Wilke-Chang correlation, presented in equation 2.18 is an empirical modification of the Stokes-Einstein equation.[39] It has been moderately successful for dilute, binary mixtures of low molecular weight non-electrolytes in liquids.[81]

$$D_{AB} = 7.4 \cdot 10^{-8} \frac{\sqrt{\Phi_B M_B} T}{\mu_B V_A^{0.6}} \tag{2.18}$$

where D_{AB} is again the diffusion coefficient, but in units of $cm^2 s^{-1}$, while A and B denote the solute and solvent, respectively. Φ_B is the association factor of the solvent, which is dimensionless, M_B represents molecular weight of the solvent in $g\ mol^{-1}$, μ_B is the solvent viscosity, but in units of $mPa \cdot s$ and V_A is molar volume in $mL\ mol^{-1}$ of the liquid solute at its ebullition point.

Siddiqi-Lucas correlation
An alternative, simplified model of the Wilke-Chang correlation was proposed by Siddiqi *et al.* This relation is applicable to aqueous solutions with a reported estimated error of 13%.[82] The correlation is given by:

$$D_{AB} = 2.98 \cdot 10^{-7} \frac{T}{V_A^{0.5473} \mu_B^{1.026}} \tag{2.19}$$

2.6.2. Microfluidic devices

To successfully perform experiments with microfluidic devices, one needs several elements: auxiliary equipment, such as pressure-driven pumps, syringes and tubing; a measurement technique to be able to study the analyte; and a detection method to monitor normal operating conditions of the device. Many possible variations of these elements exist, but the pressure-driven propulsion of fluids has been most commonly implemented.[15]

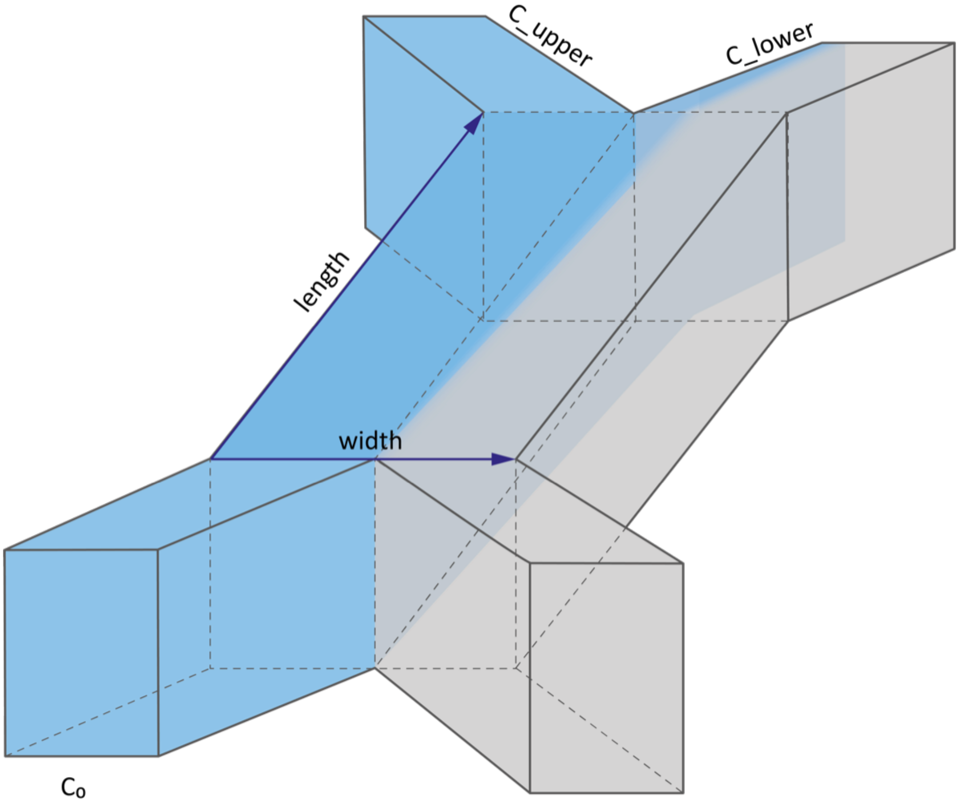

Figure 2.4: Schematic overview of single-phase diffusion in microfluidic channels.

Some parameters of importance for the amount of solute transferred from the top side to the lower side of the microfluidic channel are: the total volumetric flow rate $Q[{}^{m^3}\!/_{s}]$, the dimensions of the microchannel in 3D (Length L, Width W and Height H, all in $[m]$, and, of course, the diffusion coefficient $D[{}^{m^2}\!/_{s}]$ of the solute in its corresponding solvent, and concentration levels of the solute at each inlet, as seen in fig. 2.4. Performing such experiments yields concentration levels at the outlets of the microchannel which can be readily measured. In single-phase flows mass transfer in microchannels is generally dominated by molecular diffusion, a higher concentration at the lower outlet directly correlates to a higher diffusion coefficient. A theoretical description of this process enables estimation of the diffusion coefficient by comparing numerically obtained concentrations with experimentally obtained ones.

All of the aforementioned parameters are either known or configurable, except for the diffusion coefficient. A numerical description of this physical process could predict the diffusion coefficient accordingly.[34] Upon closer inspection of equation 2.12, it might become apparent to the reader it can be simplified when applied to a microfluidic environment. Under continuous operating conditions, mass transfer will reach a steady state, resulting in the transient term being zero. As the channel is a closed environment, with no leakage, the source term is effectively zero as well. When calculating Péclet numbers according to equation 2.13 for mass transfer in the streamwise and transverse directions, one finds that they are in the order of tens of millions and zero, respectively, due to convection being in the streamwise direction. This justifies the simplifications to consider mass transport in the streamwise direction to solely be of convective nature, and mass transfer in the transverse direction to be purely governed by diffusion. These simplifications reduce equation 2.12 to:

$$\mathbf{u}\frac{\partial C}{\partial x} = D_{AB}\frac{\partial^2 C}{\partial y^2} \tag{2.20}$$

The velocity profile obtained with lattice Boltzmann methods, can be directly inserted in the equation for mass transfer. This equation is easily discretised using finite difference methods, as described in section 2.5.1. The computational domain will consist of the microchannel only, as mass transfer only takes place here. The computational configuration is summarised in fig. 2.5.

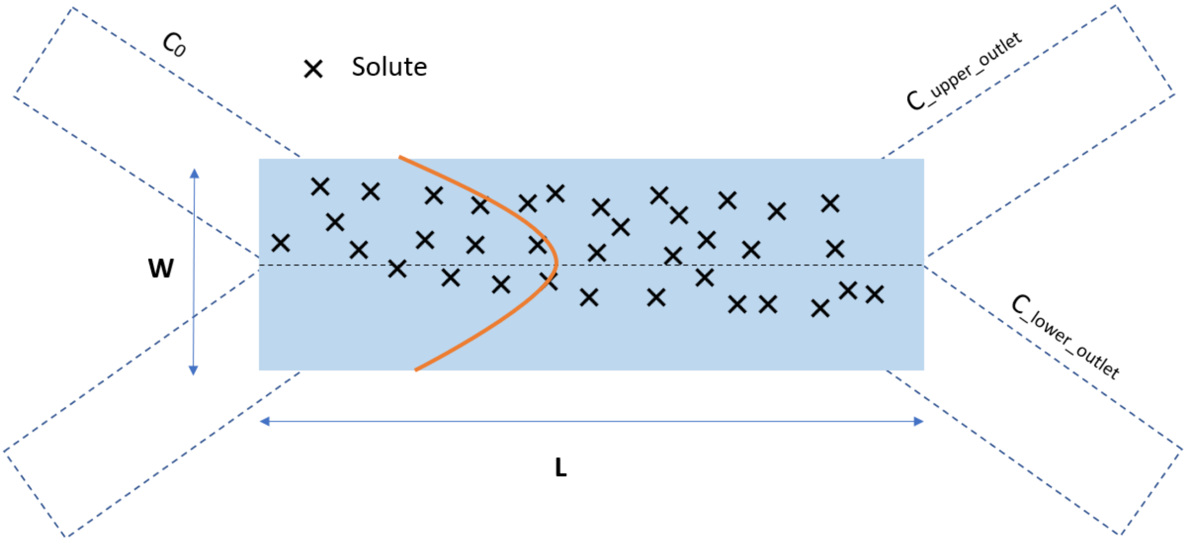

Figure 2.5: Simulation domain of mass transfer in the microfluidic channel.

When solving equation 2.20 on this domain, one obtains a value for the amount of concentration on each node. By averaging the concentration values on the column of nodes located at the outlets, one obtains the average concentrations of solute flowing into each outlet. When equation 2.20 is solved for a system with a known value for the diffusion coefficient, these numerically obtained concentrations should match the concentrations obtained when performing experiments with the corresponding solvents and solute. When the diffusion coefficient is unknown, experimentally obtained concentrations can be used as an input to a mass transfer model, and repeatedly solve equation 2.20 for a variety of values for the diffusion constant, until the numerically obtained concentrations match the experimentally obtained ones to within the desired tolerance.

2.6.3. Detection methods of solute concentrations

One exemplary detection method for concentrations at the outlets is UV-Vis spectrophotometry. It is a chemical analytic method that determines the concentration of a substance in a sample by measuring absorption of a wavelength of light λ between 200 and 800 nm.[83] The absorbance A, in Absorbance Units $[AU]$, is expressed as:

$$A = -log_{10}({}^{I}/{}_{I_0}) \tag{2.21}$$

Where I is the measured light intensity, and I_0 the initial light intensity produced by the spectrometer. The absorbance is linearly correlated to the concentration C by:[84]

$$C = \frac{A}{\epsilon \cdot d} \tag{2.22}$$

where ϵ is the extinction coefficient, and d the pathlength of the light traveling trough the absorbing medium. The extinction coefficient is generally determined by setting up calibration curves, which uncovers the linear relationship between the absorbance A and the concentration C.

3

Methodology

This chapter describes all experimental procedures and numerical methods used in this study. It provides an overview of all materials necessary to perform adequate experiments. It illustrates how the experimental methods have lead to obtaining values for concentrations at the outlets of the microchannel by first providing a brief general overview, after which it is further elaborated upon. Subsequently it reports how the described computational methods were applied to a microfluidic environment, and it will conclude with how both experimental and numerical techniques were combined to make an estimation for the diffusion coefficient.

3.1. Materials

3.1.1. Instruments & equipment

An overview of relevant instruments used for this research

Table 3.1: List of instruments used.

Instrument	Manufacturer	Type	Notes
Syringe pump #1	Braintree Scientific, Inc.	8002X	-
Syringe pump #2	Harvard Apparatus	Pico Plus Elite 70-4506	-
Syringes	TERUMO	SS*02LE1 2.5mL	-
Microfluidic channel #1	Micronit	H50.015.2	-
Microfluidic channel #2	IMT	ICC-DY15G	-
Tubing #1	INACOM Instruments	Tub PFA	-
Tubing #2	IMT	ICT-55P	PEEK tubing
Microscope #1	Mustcam	UM038.	LCD Digital Microscope
Microscope #2	Euromex	NA0.30 WD72	-
Vortexer	Scientific Industries SI^{TM}	Vortex-Genie^{TM}2	-
UV-Vis #1	VWR	UV-6300PC	Spectrophotometer
UV-Vis #2	Hach Lange	DR 5000	Spectrophotometer
Cuvettes	Purshee Experiment	Quartz Absorption Cells	-
^{68}Ge/^{68}Ga Generator	Eckert & Zirgler	IGG100 GMP	-
Automatic gamma counter	PerkinElmer, Inc.	Wallac Wizard^2	-
Capillary viscometer	SI Analytics	Type 509 04	-

3.1.2. Chemicals

A short overview of all chemicals used in this research is provided in Table 3.2

Table 3.2: List of used chemicals.

Chemical	**Specification/Chemical name**	**Supplier**	**Purity**
$Zn(NO_3)_2 \cdot (H_2O)_6(s)$	Zinc Nitrate hexahydrate	Acros Organics	98%
$HCl(aq)$	Hydrochloric acid solution	Merck	30% (w/w)
HNO_3	Nitric acid	Honeywell | Fluka	$\geq$65% (w/w)
$C_{14}H_{18}ClN_3S \cdot nH_2O$	methylene blue	J.T. Baker Chemicals B.V.	'Baker' *Grade*
H_2O	Ultrapure water	Milli-Q	R = 18.2MΩ

3.2. Measurement method

The method was first sought to be validated with measurements of diffusion coefficients of some selected components with diffusion coefficients found in literature, such as methylthioninium chloride, commonly known as methylene blue, in water, which several authors have investigated. Miložič *et al*. found it to be $4.6 \cdot 10^{-6} cm^2/s$, using similar estimation methods as presented in this study.[34]. Chakraborty *et al*. reported the diffusion coefficient to be $5.7 \cdot 10^{-6} cm^2/s$[85] and Vetter *et al*. presented a value of $7.6 \cdot 10^{-6} cm^2/s$,[86] both exploiting cyclic voltammetric methods.

3.2.1. General setup

The general setup consisted of a syringe pump, a microfluidic device, which is monitored visually with a digital microscope, and collection vials. A schematic overview can be found in fig. 3.1. Syringe A contains the selected solvent and solute, while syringe B contains solvent only. The syringes were placed in their selective syringe pumps, which are flow rate configurable, and connected to the inlets of the microfluidic channel. The solutions were collected in sample vials, while the channel flow was visually inspected with a digital microscope.

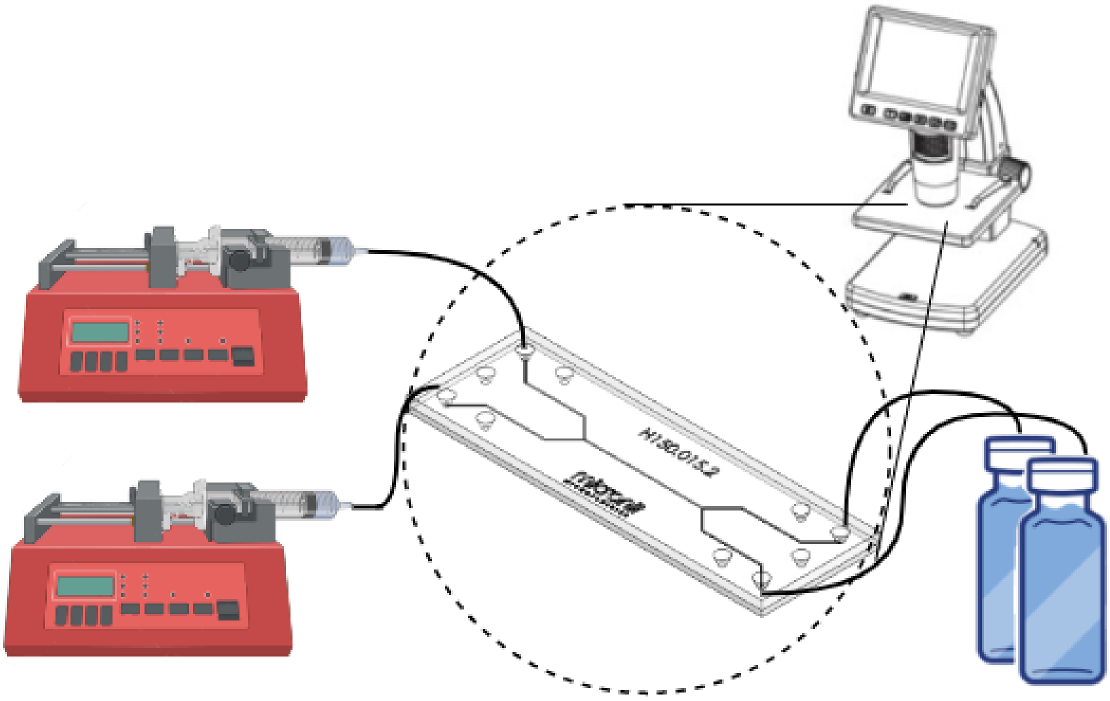

Figure 3.1: An overview of the experimental operation of a microfluidic device. It consists of configurable syringe pumps, where syringe A is placed in the upper syringe pump displayed in the figure, and syringe B in the lower syringe pump. The setup also includes the microfluidic device itself, a visual inspection method and collection vials.

3.2.2. Microchannel dimensions

Two microchannels of slightly different geometrical cross-sections and lengths were investigated, revealing whether the setup is of any significance on the acquired results. Microchannel dimensions are obtained through their manufacturing blueprints. The cross-sections are shown in Fig. 3.2. Microchannel #1 has a length of 15 mm, and microchannel #2 has a length of 120 mm. The areas of the microchannels are approximated numerically by the orange overlay in fig. 3.2, fully describing the diffusion surface, while not altering the surface area of the channel.

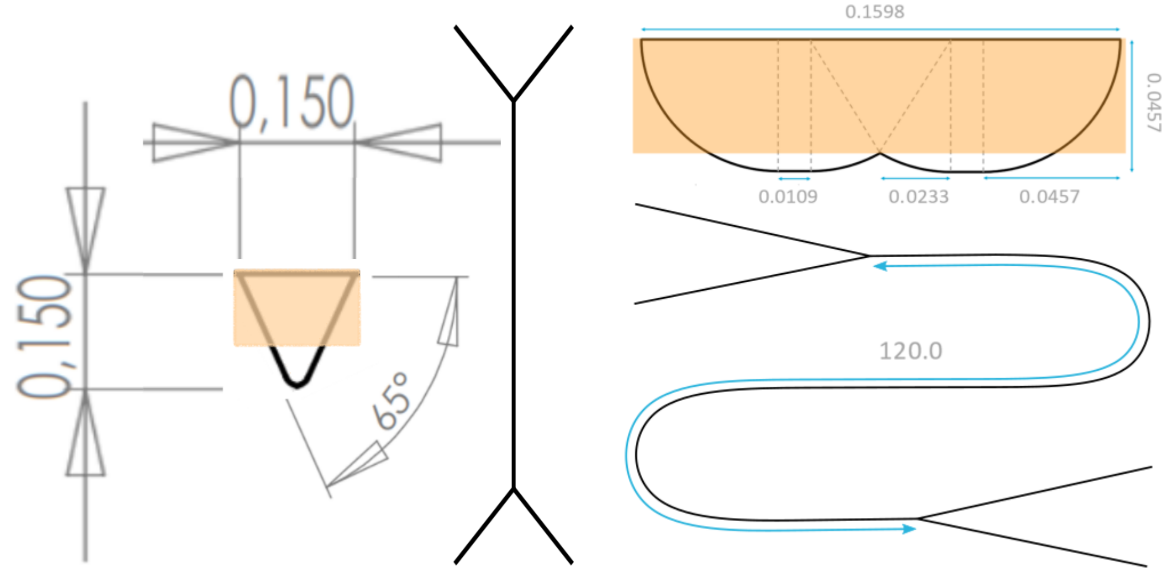

(a) Triangular cross-section microchannel 1. The triangular area is approximated by a rectangle (shown in orange) of width W = 0.15 mm, and height H = 0.1125 mm. The length of this microchannel is 15mm.

(b) Cross-section microchannel 2, revealing a flow-guided structure. The diffusion area indicated by the orange box, is approximated with width W = 0.160 mm, height H = 0.0393 mm. The length of this particular microchannel is 120 mm.

Figure 3.2: Microchannel cross-sections as supplied by their respective manufacturers. All dimensions are in mm.

3.3. Experimental procedure

3.3.1. Methylene blue

The experiment was performed by filling a 2.5 mL syringe with a aqueous solution of 3 mM methylene blue and another with ultrapure water. Both syringes were connected to tubing with a Luer-Lock system, and placed in syringe pumps. Flow rates were set equal on both pumps in the range of 13-40 $\mu L\, min^{-1}$. The system was allowed to equilibrate for 15 minutes before samples were taken in regular intervals of 10 minutes. All sample vials were weighed before and after collection of the sample, to indirectly verify whether the average flow rates from both outlets were equal to the set flow rate, and each other. This did not account for any pulsation in the flows. For determining the concentrations of methylene blue at the inlet and both outlets, UV-Vis photospectroscopy with a Double Beam UV-Vis-spectrometer was used, for which a calibration line for concentrations between 2-20 μM for wavelengths λ = 600 nm and λ = 663 nm was constructed, using linear regression. 1050 μL of accordingly diluted aqueous solution of methylene blue was filled in quartz cuvettes of equal volume. The absorbance A was measured at both wavelengths, from which the concentration C was extracted according to the calibration curves. The experiments were performed at least thrice, and were repeated for both microchannels displayed in fig. 3.2.

3.3.2. Gallium-68

Aqueous solutions with zinc concentrations ranging from 1 M to 4 M, dissolved in different concentrations of nitric acid, ranging from 0.01 M to 1 M were investigated. The solutions were prepared by first diluting nitric acid to the desired concentrations with ultrapure water, before dissolving the appropriate amount of zinc nitrate in them. ^{68}Ga was produced with a ^{68}Ge/^{68}Ga generator, of which activities of roughly 50 MBq were extracted in 5 mL 0.1 M hydrochloric acid dissolved in water. 10 μL of this solution was added to 2.5 mL zinc nitrate solution. The experimental procedure is identical as that of methylene blue. The set flow rates for each inlet were between 10-13 $\mu L\ min^{-1}$, to account for an expected lower diffusion rate. Concentrations were evaluated using an automated gamma counter, where the energy detection window was set to 400-600 keV.

3.4. Numerical model development

Häusler *et al.* showed that mass transport in a microfluidic channel in a 2D description, matches the results acquired with 3D descriptions,[33] specifically the difference in calculated outlet concentrations were less than 0.1%. As such, this study concerned itself with numerical models in 2D exclusively.

3.4.1. Velocity equation

The following equations will thus be approximated by the solution to the discretised lattice Boltzmann equation as presented in equation 2.9. The domain is generated in the form of a 2D Boolean array, as demonstrated in fig. 3.3

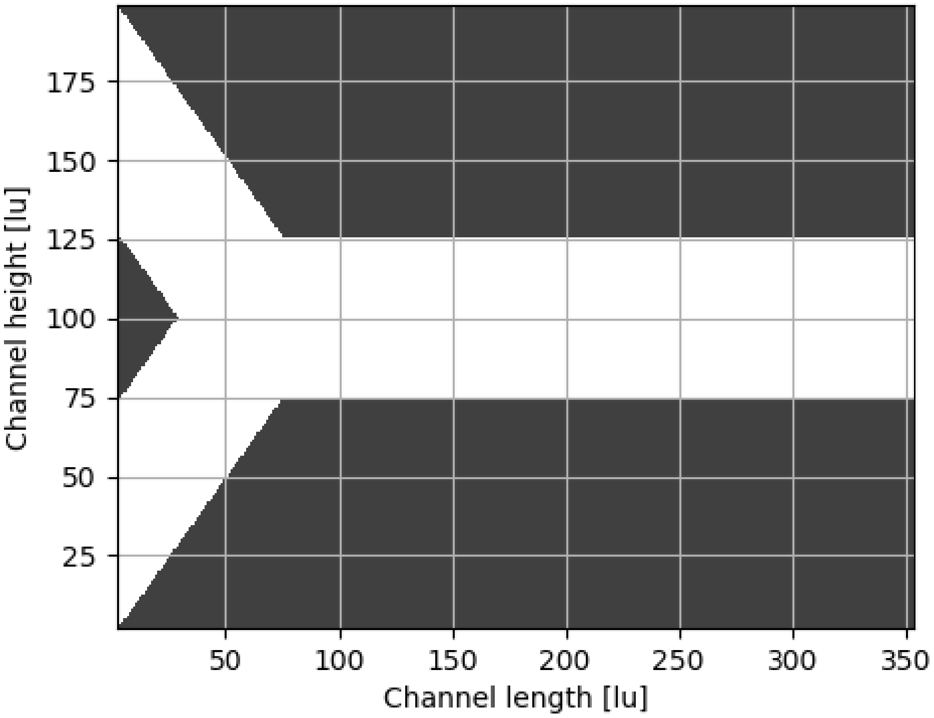

Figure 3.3: Boolean array representing the simulation domain as a Y-shaped microchannel inlet.

At the microchannel walls a no-slip ($\mathbf{u} = \vec{0}$) Dirichlet boundary condition is applied, according to the half-way bounce back method first introduced by Ladd *et al.*[87] The inlet boundary conditions are to be defined as the average velocity derived from the set volumetric flow rate according to a slightly modified half-way bounce back method,[88] while at the outlet a convective boundary condition as described by Lou *et al.*[89] As bounceback methods are implemented here in combination with the simplified collision operator described in equation 2.10, special care must be taken for choosing the relaxation parameter τ. It is set to be $\tau = \sqrt{3/16} + 1/2$, as this places the physical boundary exactly halfway between the boundary and fluid nodes of the computational domain, rendering the solution to be third-order accurate, when the direction of the flow coincides with the direction of discretisation.[90,91]

3.4.2. Mass transfer equation

The boundary conditions implemented at the inlets are defined according to figure 3.4, with Neumann boundary conditions constructed from a first order forward and backward difference with first order accuracy was implemented along the bottom and top microchannel walls, respectively. The outlet was also by defined as a first order backward Neumann boundary condition, to first order accuracy.

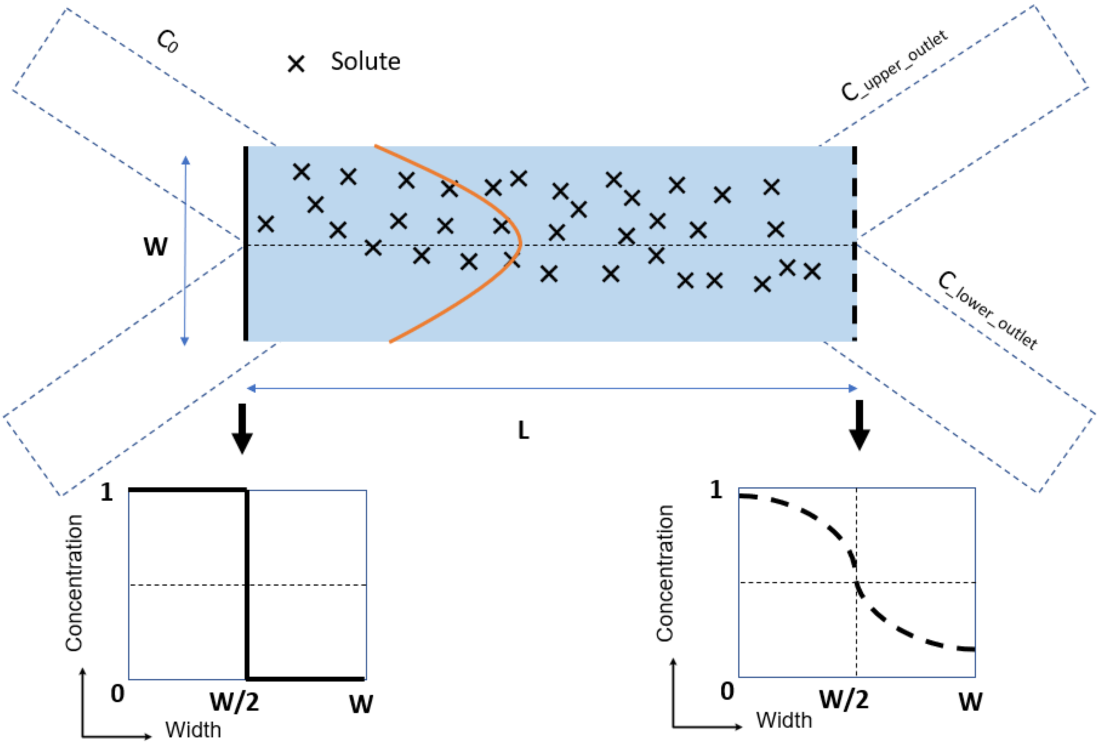

Figure 3.4: Visualisation of implemented boundary conditions for mass transfer description in microfluidic channels. At the inlets a sharp step function is defined, to simulate an assumed uniform distribution of solute flowing in from the top inlet into the microchannel. This step function is expected to diffuse into similar profiles as represented by the graph with the dashed line on the right.

Concentrations of the solute at the outlets of the microchannel were subsequently obtained by integrating over the concentration profile at this particular location. Equation 2.20 was solved on the domain indicated by the shaded area in fig. 3.4, with a guessed value for the diffusion coefficient. The diffusion coefficient was then altered manually and the equation was solved again, until the numerically obtained concentrations at the outlets matched the experimentally observed concentrations to within 0.1%.

4

Results & Discussion

In this chapter the results of the previously described experiments are presented and discussed. All experiments have been performed between two to five times, and the reported associated error or the size of the error bar is one standard error of the mean.

4.1. Velocity equation

4.1.1. Verification of the lattice Boltzmann method

The lattice Boltzmann model has been benchmarked to verify whether it complies with known analytical results. Two examples of benchmarking problems are the Couette flow, and the development of a Poiseuille flow profile as mentioned in chapter 2. Couette flow is where an incompressible fluid lies between two infinite parallel plates, the upper of which moves with a velocity $\mathbf{u}_0$, and the lower plate is fixed in space, where a no-slip condition ($\mathbf{u} = 0$) is applied. Poiseuille flow is the analytical solution to equation 2.6 on a semi-infinite rectangular domain, with no-slip boundary conditions along the channel walls. These problems are further described in great detail by Krüger *et al.*[71] The analytical solutions for the velocity profiles, as indicated by the dashed lines in fig. 4.1, match the numerical computed solutions, at least for a range of Q = 20-80 $\mu L\ min^{-1}$, with an error of $\leq$ 1%, which deems the lattice Boltzmann model suitable for further use.

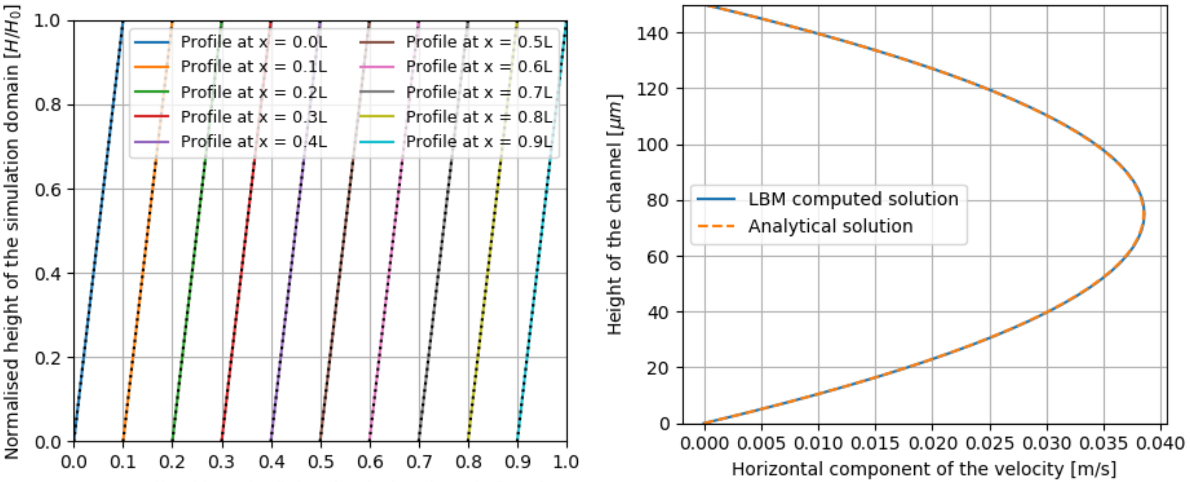

(a) Couette flow on a rectangular domain, with an imposed velocity of 0.001 [lu/ts] at the upper wall. The analytical solutions are presented as the dashed lines.

(b) Poiseuille flow in the short, triangular microchannel. The figure shows a comparison between the solution numerically computed with the lattice Boltzmann model, and the analytical solution obtained with equation 2.6 for Q = 26 $\mu L\ min^{-1}$

Figure 4.1: Benchmark problems which have analytical solutions to verify the accuracy of the lattice Boltzmann method

4.1.2. Fluid flow in the microchannel

The streamlines of the converged fluid flow in microchannel #1, computed with the lattice Boltzmann method, is seen in Fig. 4.2. The length of the inlet channels are in the same order of magnitude as the width of the microchannel. The streamlines merge together as expected, as the maximum velocity in the microchannel is 3 times the average velocity imposed on the left boundary of each inlet, in complete accordance with the 2D description of Poiseuille flow.[92] This holds true for at least a range of flow rates of Q = 10-40 $\mu L\ min^{-1}$ for each inlet. For the microchannel itself the first millimeter in the lengthwise direction is modelled, accompanied by an open boundary condition. This typically gives rise to small inaccuracies, as the physics is not known outside this computational boundary.[93] Lou *et al* described several methods for implementing an outflow boundary condition, without distorting the velocity profile significantly, for multi-phase flows in microfluidic channels. Of the methods described, they found a convective outflow boundary condition with the average velocity as the characteristic velocity performed best.[89] This holds also true for the single-phase flow in this study, although this method is not completely free of numerical artefacts, as the streamlines bend outward at the outlets. Small numerical errors are expected at a simulated open boundary.[93] However, these numerical errors can be circumvented by determining when the numerical solution has sufficiently converged to the analytical solution in the microchannel, and cutting the solution off at this point, well before any numerical discrepancies become significant.

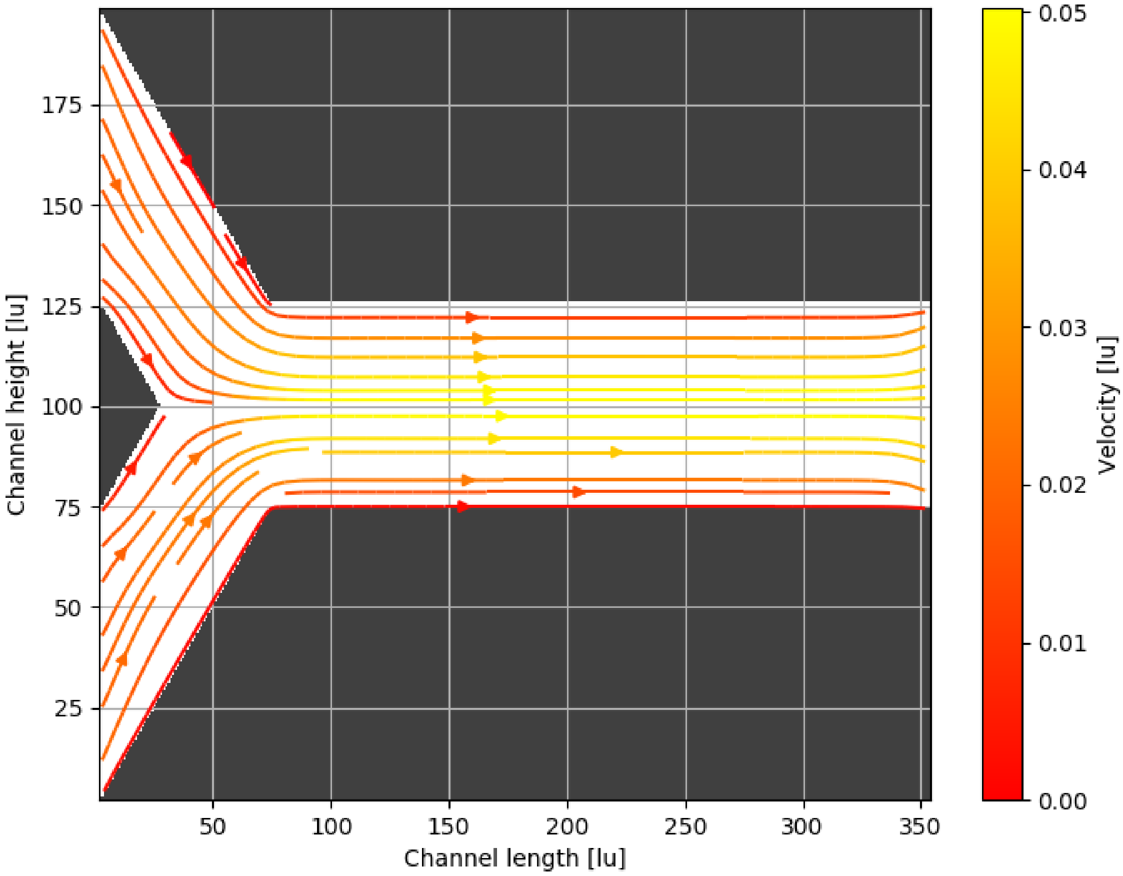

Figure 4.2: Fully developed flow in microchannel #1, with Y-shaped inlets. The figure indicates the solution to inlet conditions of an an average flow rate of Q = 40 $\mu Lmin^{-1}$, expressed in lattice units.

Fig. 4.3 shows a similar plot for the horizontal component of the velocity. When further inspecting the development length of the profile in Fig. 4.4, it shows that the horizontal velocity profile converges to the analytical solution within 2.5% of the length of the channel, which is well below the development length of the flow empirically described by Dombrowski *et al*.[94] This suggests that assuming a developed velocity profile throughout the entire length of the channel is a legitimate simplification. The effect of this short development length is investigated further in section 4.4.

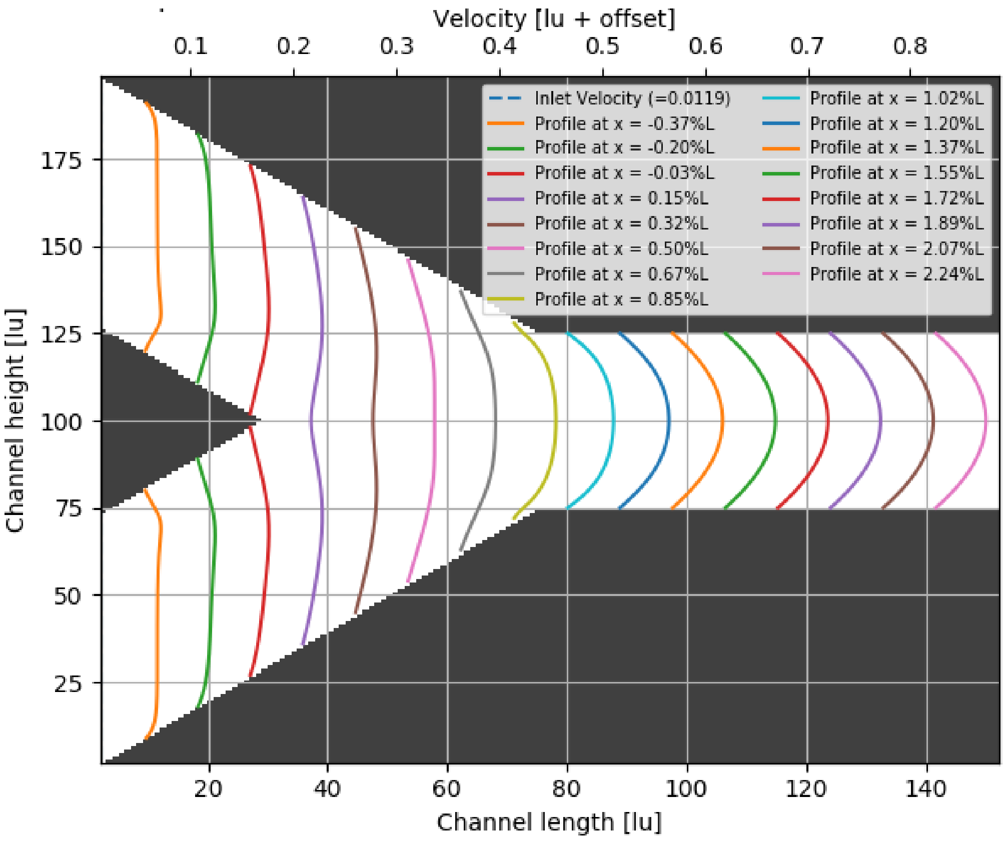

Figure 4.3: Development of the horizontal component of the velocity field at the inlets of the Y-shaped microchannel (microchannel #1) at t = 10.392 ms

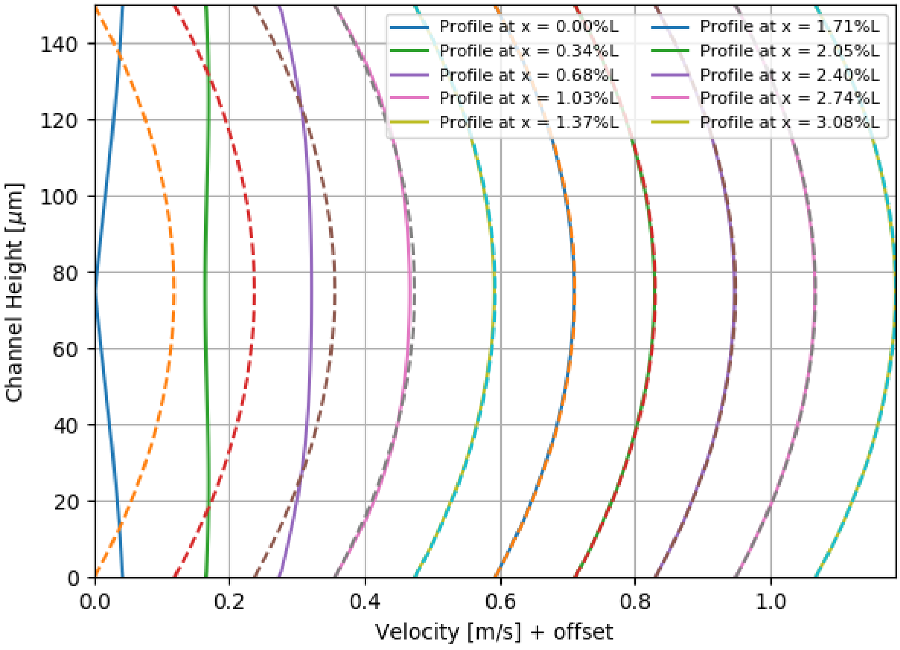

Figure 4.4: Comparison of the lattice Boltzmann computed solution to the analytical solution, within 1.5% of the entire length of microchannel #1, which has a physical length of 15 mm.

4.2. Mass transfer equation

The mass transfer section has been verified visually by determining the concentration profiles at both ends of the microfluidic channel. Fig. 4.5 shows the solved concentration profile in the micro channel on the computational domain as indicated in fig. 2.5. The concentration profile at the inlet is defined as shown in fig. 4.6a. The profile is not a perfectly sharp step function due to the height of the microchannel being discretised in an odd number of nodes, where the concentration on the middle node is defined as $C = {}^{C_0}/_{2}$. This discretisation in an odd number of nodes allows for a perfectly symmetrical velocity flow profile. Concentrations at the outlets can be determined by integrating over the concentration profile at the upper and lower outlet respectively, as seen in fig. 4.6b.

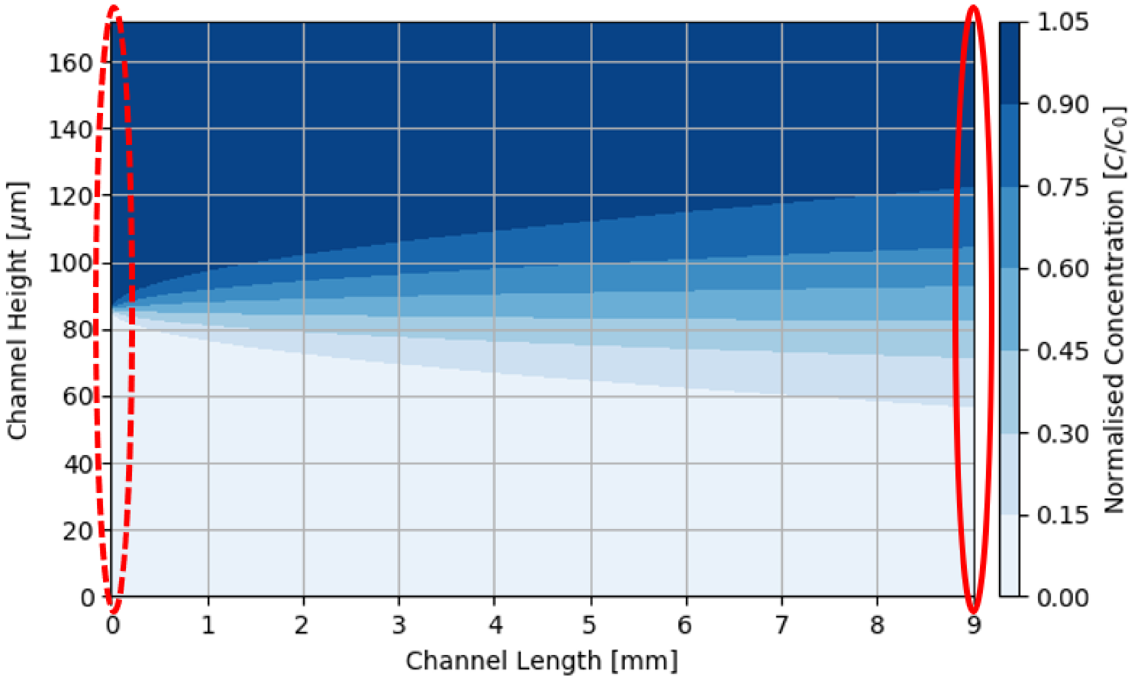

Figure 4.5: Visualisation of the computed mass transfer in the microfluidic channel. Dimensions are H/W = 100/172μm, L = 12.5mm, flow rate at each inlet is 20 $\mu L\ min^{-1}$ and D_{AB} = 13.5·$10^{-6} cm^2\ s^{-1}$. The dotted circle on the left indicates the inlets, and the full circle on the right illustrates concentration distribution at the outlets.

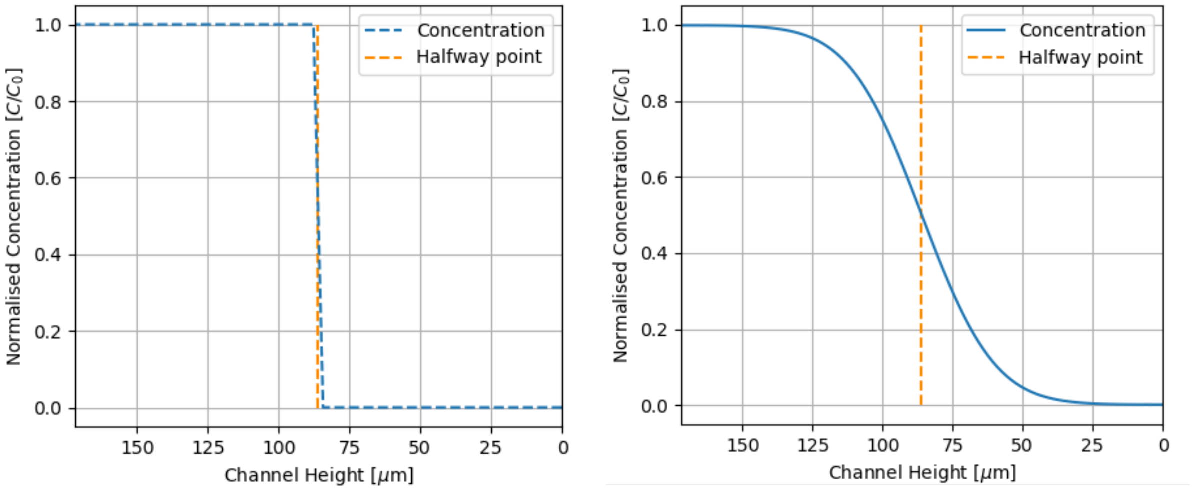

(a) Concentration profile imposed at the inlets of the microchannel, at the position indicated by the dotted circle in fig. 4.5

(b) Developed concentration profile at the outlets, at the position indicated by the full circle in fig. 4.5

Figure 4.6: Concentration profiles at the inlets and outlets of the microfluidic channel

Fig. 4.6b can be directly compared to the results presented by Miložič *et al.*[34] Visual inspection, as presented more clearly in fig. 4.7. This shows that this result matches their results for the concentration profiles for the implicit Finite Difference method only. Implicit and explicit methods converge to the same solution, as long as the mesh size on which it is solved is sufficiently small.[78] This could suggest their explicit model was solved on a grid too coarse to obtain fully accurate results. For the implicit model it can be stated that the 2D model yields similar results to their 3D model, in accordance with the results of Häusler *et al.*[33]

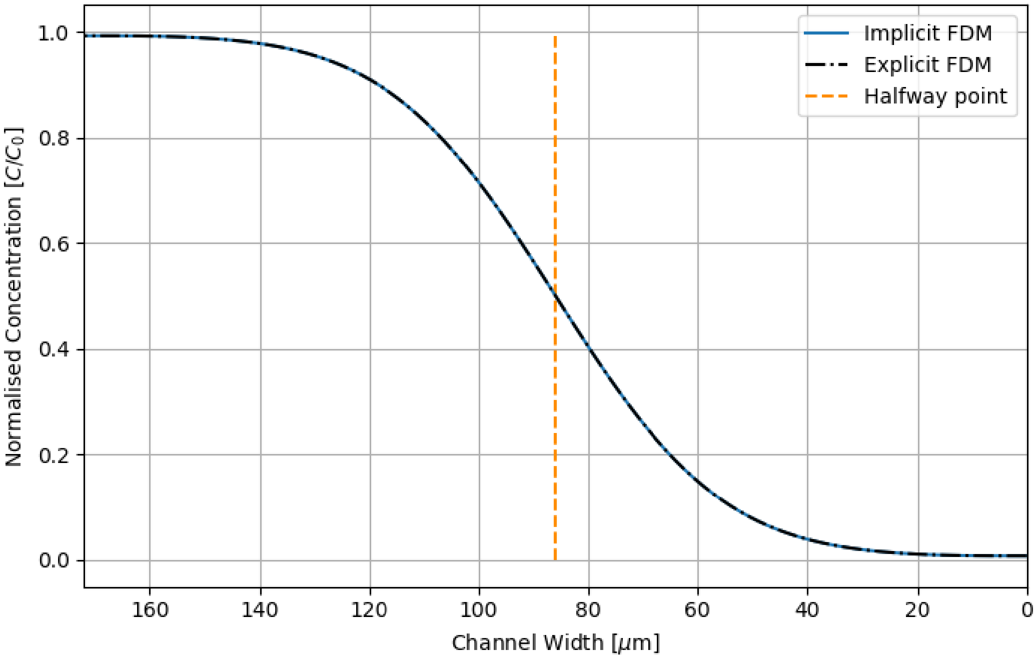

(a) Developed concentration profile at the outlets, as numerically computed by the methods as presented in this study.

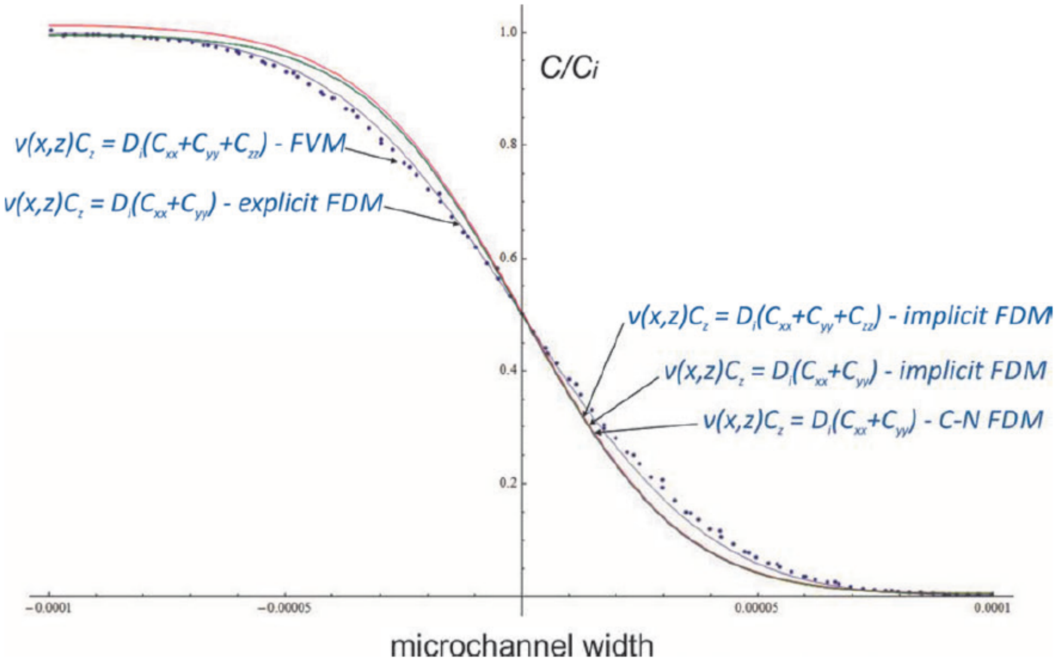

(b) Developed concentration profile at the outlets, as numerically computed by Miložič *et al.*[34]

Figure 4.7: Direct comparison of numerically computed concentration profiles at the outlets of a microfluidic channel with dimensions H/W = 100/172μm, L = 12.5 mm. The flow rate Q at each inlet is 20 $\mu L\ min^{-1}$ and the diffusion coefficient D_{AB} = 13.5$\cdot 10^{-6} cm^2\ s^{-1}$ with the results presented by Miložič *et al.*[34]

4.3. Solute concentration measurements – UV-Vis

The detection wavelength was chosen based on the absorbance spectrum of methylene blue[95], as seen in fig. 4.8.

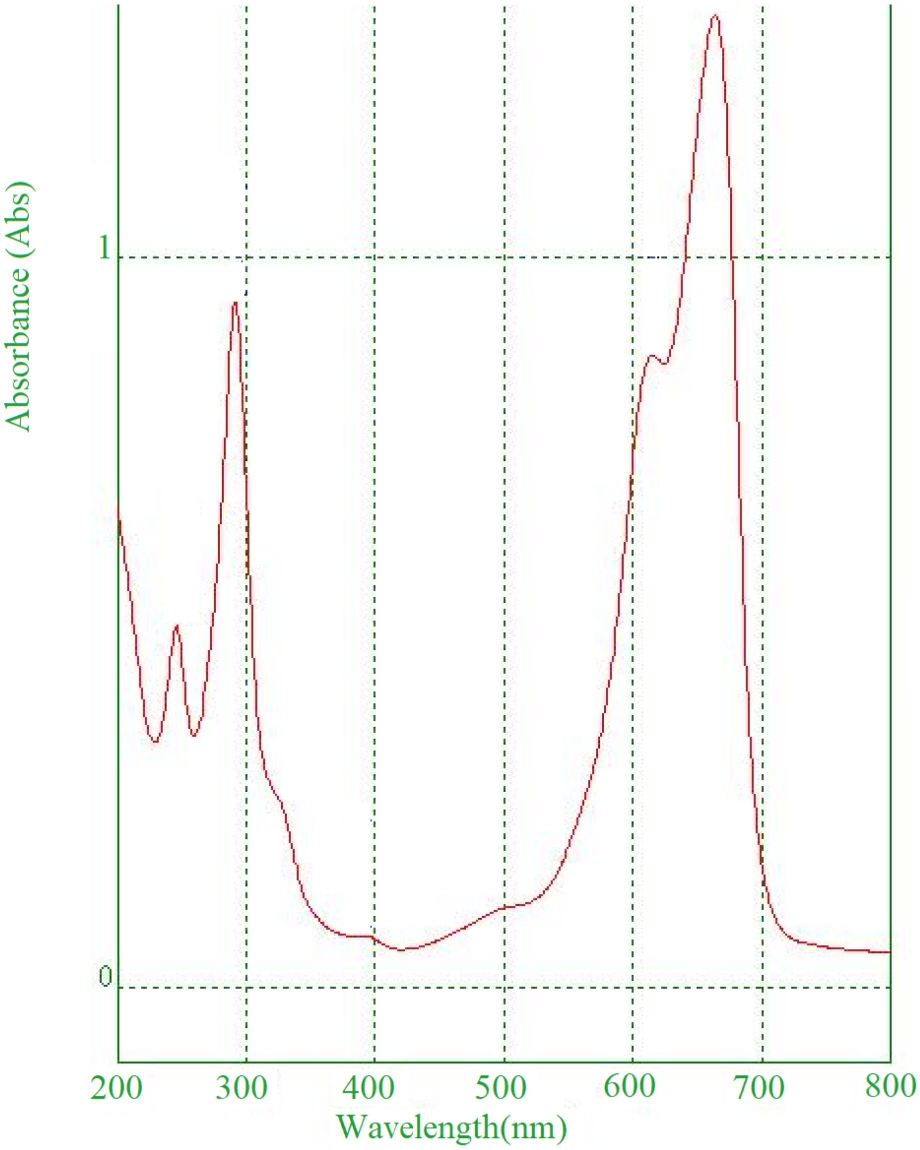

Figure 4.8: Absorption spectrum of an aqueous solution of methylene blue. This particular spectrum corresponds to the mesomer II variant of the monomer[96]

Even though the absorbance spectrum shows peaks at λ = 245 nm, λ = 291 nm, and λ = 664 nm, the peaks residing within the visible light spectrum were chosen, due to observed breakdown of methylene blue compound at UV-light wavelengths.[97] The chosen wavelengths specifically wereλ = 600 nm, as this allows for direct comparison with literature,[34] and λ = 663 nm, as it shows a maximum absorbance there, meaning it can still accurately measure concentrations even for $C < 10\ \mu M$.[98]

4.4. Experimental results for methylene blue

Diffusion in the microchannel was visually inspected, to verify whether a flat diffusion surface could be achieved by the setup as proposed in fig. 3.1. These results are summarised in fig. 4.9. Figures 4.9a & 4.9b show a slight increase in the diffusion front for slower flow rates, whereas the diffusion front for microchannel #2 is barely noticeable. This suggests that diffusion is the sole cause of mass transport in the transverse direction, but one should not draw any quantitative conclusions from these images.

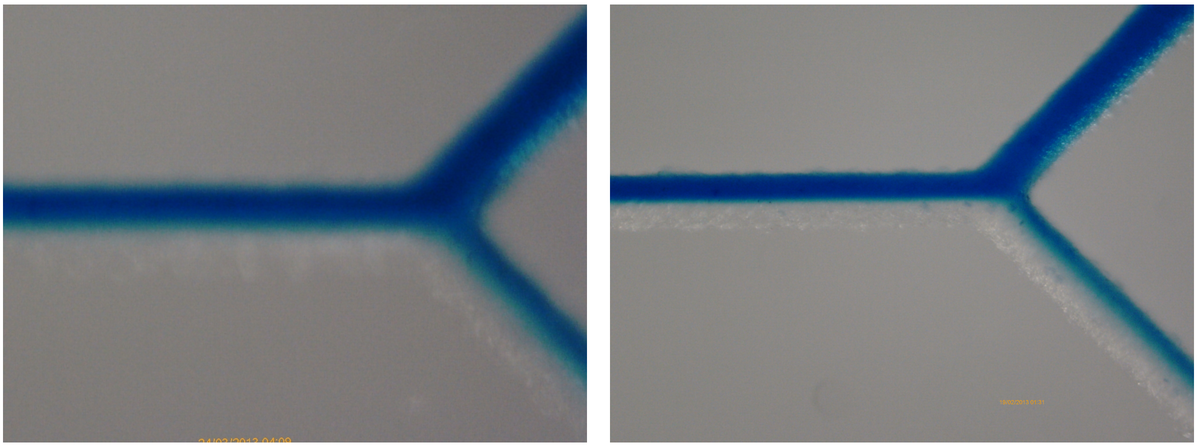

(a) Diffusion front close to the outlets of microchannel #1. Set flow rates were 13 $\mu L min^{-1}$ for each inlet. Image was obtained with microscope #1

(b) Diffusion front close to the outlets of microchannel #1. Set flow rates were 40 $\mu L min^{-1}$ for each inlet. Image was obtained with microscope #1

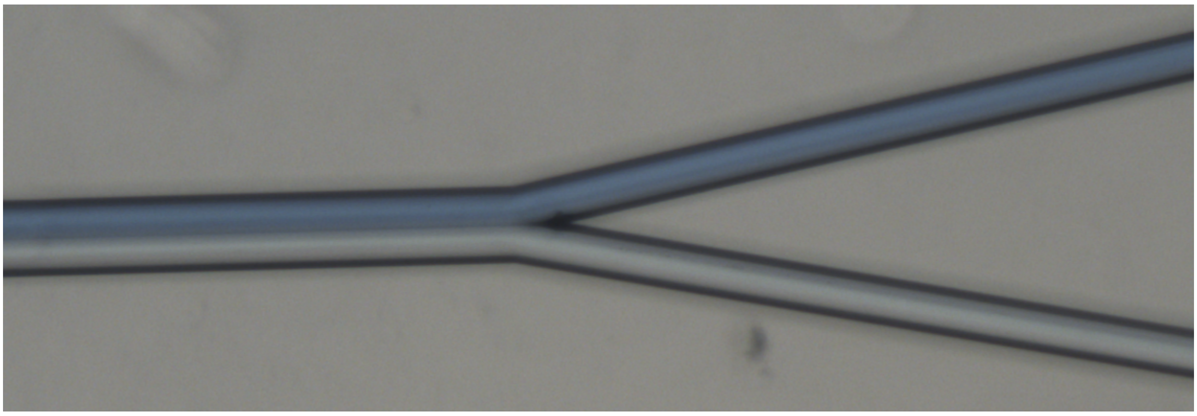

(c) Diffusion front close to the outlets of microchannel #2. Set flow rates were 40 $\mu L min^{-1}$ for each inlet. Image was obtained with microscope #2

Figure 4.9: Visualisations of the diffusion front of methylene blue in an aqueous solution. Microchannel #1 was imaged for 13 $\mu L\ min^{-1}$ and 40 $\mu L\ min^{-1}$. Microchannel #2 was imaged for 40 $\mu L\ min^{-1}$ with microscope #2.

The setup was verified for varying flow rates and microchannel design, varying one at a time while keeping others constant, to determine their effects on the obtained concentrations at the outlet. The importance on obtaining reliable results for the concentration is emphasised here, as this is direct input for the estimation of the diffusion coefficient. As such, stable operational and process conditions are required to ensure mass transport of the solute from one inflow to the other outflow is by diffusion only. To establish a continuous flow with minimal pulsations, the microchannels were to be thoroughly flushed with the selected solvent, to prevent the accumulation of filth at the outlets, as seen in fig. 4.10.

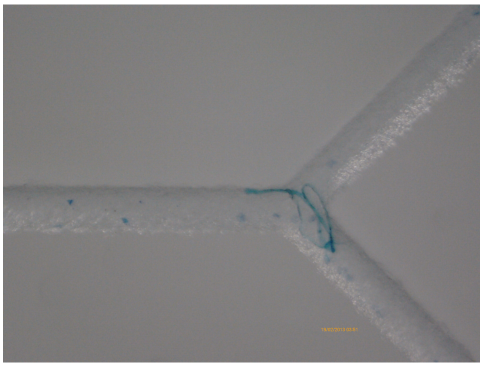

Figure 4.10: Accumulation of filth at the outlets of microchannel #1.

The average flow rates from each outlet were passively measured by assessing the weight of the sample collected, and recording the amount of time taken for each experiment. These flow rates were expected to be fully equal, as this would indicate mass transfer to be by diffusion only. Perfectly equal flow rates were not achieved consistently, especially with syringe pumps used in setup #1. Results where flow rates deviated more than 5% from their set value were deemed too inaccurate and were discarded.

Another thing to note is that some slight deviations in reference measurements were observed. The initial concentration C_0 was fixed at 3.07 mM for all experiments, and for certainty a triplicate reference measurement of this initial concentration has been performed with both UV-Vis machines, for both wavelengths specified in section 3.3.1. The reference stock solution was diluted by a factor of 600, carefully noting the weights at each dilution step, such that expected concentration value fell within the bounds of the calibration curves, as described in section 3.3.1. Before each measurement, the diluted solutions were vortexed for one minute each. These reference measurements have been summarised in table 4.1.

Obviously these results do not match expectations, as the measured values for the concentrations do not add up to the concentration of the prepared solution. Such fluctuations in the absorption spectra can be attributed to self-aggregation of the methylene blue molecules and temperature dependence, as described by Fernández Péral *et al.*[96,99], or due to degradation of the compound as a result of exposure to environmental sunlight.[97]. Dilution errors were systematically $\leq$ 1%, due to the accuracy of the balance used. Despite these oscillations in reference concentrations, the standard errors in the fractional concentrations at the outlet never exceeded 1% for each setup at each wavelength, which is further explored in table 4.2.

Table 4.1: An overview of all reference measurements performed with UV-Vis machines used in both measurement setups

UV-Vis #	**Wavelength** λ **[nm]**	**Initial Concentration [mM]**	**Measured Concentration [mM]**
1	600	3.07	2.36 $\pm$ 0.04
1	663	3.07	2.98 $\pm$ 0.03
2	600	3.07	3.63 $\pm$ 0.01
2	663	3.07	3.70 $\pm$ 0.01

Next, the concentration levels as measured at the outlets were compared with the reference concentrations, and it was found that these matched the initial concentration as indicated by the reference measurements within 2% for experiments 2-5, and for experiment 1 an average deviation of 3.5% was observed. When this deviation is small, the initial concentration can be approximated as:

$$C_0 = C_{upper\_outlet} + C_{lower\_outlet} \tag{4.1}$$

This proves useful, especially when the initial concentration is unknown, or if the reference measurements are off. The right-hand side of equation 4.1 alleviates the problems arising due to mismatching concentrations.

The results have been summarised in table 4.2. All experiments have been performed under ambient temperatures, with T = 19-20 $^\circ C$. The first thing to note is that all presented values for the fraction of solute diffused, is determined by averaging over the measurements performed with wavelengths at λ = 600 nm and λ = 663 nm, as the differences in measured concentrations were consistently $\leq$ 1% when employing equation 4.1. Secondly, the impact of the numerically calculated lattice Boltzmann velocity profile is shown to be less than 1% on the estimation of the diffusion coefficient for microchannel #1. For further experimentation with both microchannels a fully developed flow was assumed. Furthermore it is observed that for experiments #2-5, the found values for the diffusion coefficient are between 12.1 $\cdot 10^{-6} cm^2 s^{-1}$ and 13.6 $\cdot 10^{-6} cm^2 s^{-1}$ and an outlying value of D = 8.3 $\cdot 10^{-6} cm^2 s^{-1}$ for experiment #1. This shows that the method is quite sensitive to experimental errors, but when stable operating conditions have been achieved, they remain stable for the duration of the experiment. Experiment #1 and experiment #4 have been performed in an identical manner, but with different equipment, and the measured concentrations at the outlets deviate just 5% from each other, resulting in almost a 50% deviation in the obtained diffusion coefficient. This strongly emphasises the necessity of performing experiments with great accuracy. The source of this particular deviation could be explained by simultaneous and equal leakage from the co-flowing streams, perhaps caused by the surface roughness of microfluidic channel #1, and having avoided error detection by measuring the average flow rates of both streams, due to equal amounts of leakage.

Table 4.2: Diffusion coefficients of methylene blue in ultrapure water.

Experiment	**Setup**	**Microchannel**	Q_{total} [$\mu L min^{-1}$]	$Q_{deviation}$ **of setpoint**	**Outlet of microchannel**	**Fraction of total counts (mean + sem) [n=3-5]**	**Estimated D (analytical velocity profile) [$10^{-6} cm^2\ s^{-1}$]**	**Estimated D (LBM velocity profile) [$10^{-6} cm^2\ s^{-1}$]**
#1	1	1	26	0.8%	Upper	84.81 ± 0.37%	8.3 ± 0.3	8.3 ± 0.3
					Lower	15.19 ± 0.37%		
#2	1	1	80	2.6%	Upper	89.64 ± 0.06%	13.6 ± 0.0	13.5 ± 0.0
					Lower	10.36 ± 0.06%		
#3	1	2	80	1.4%	Upper	81.34 ± 0.19%	13.6 ± 0.2	–
					Lower	18.66 ± 0.19%		
#4	2	1	26	2.8%	Upper	80.57 ± 0.43%	12.1 ± 0.4	12.1 ± 0.4
					Lower	19.43 ± 0.43%		
#5	2	2	80	1.5%	Upper	82.22 ± 0.13%	12.7 ± 0.1	–
					Lower	17.78 ± 0.13%		
Mean	-	-	-	-	-	-	12.0 ± 1.0	–

Another thing to note is the large discrepancy with the diffusion coefficient values found in literature,[34,85,86]. This holds especially true for the value of 4.6 $\cdot 10^{-6}$ $cm^2 s^{-1}$ found by Miložič *et al*, which is almost a factor of three lower, since the numerical model is assumed to be adequately validated by the results as presented in fig. 4.7. Miložič *et al.* are not specific about their method on how to extract the diffusion coefficient from the numerical model, and neither present their experimental parameters from which their value for the diffusion coefficient is obtained, thwarting the ability to directly compare these. What can be noted, is that they propose the use of the *explicit* finite difference method to solve for the mass transfer in the channel, while fig. 4.7 shows a small discrepancy for their explicit finite difference method. This discrepancy between their explicit and implicit finite difference methods can be simulated by increasing the length of the microchannel by 20%, as seen in fig. 4.11, which directly corresponds with an error of 20% for the estimated diffusion coefficient. This suggests that even seemingly small deviations in the concentrations curves at the outlets, can have a large impact on diffusion coefficient estimation. They also state a contradiction in their presented paper, namely they specify the length of their microfluidic chip, the H-cell, to be of length 33.2 cm and later on they specify it to be 66 cm. This factor of 2 combined with the 20% error induced by their explicit finite difference method, could explain the discrepancy. These errors could all be coincidental, but it does leave some doubts to the validity of their results. They also use similar empirical correlations for estimating the diffusion coefficients as described in section 2.6.1, but these results could not be reproduced, mainly due to unavailable data on the molar volume of methylene blue at its boiling point, as the compound decomposes before reaching the required temperatures.[100]

The results also do not show agreement with the reported diffusion coefficients of methylene blue in water, of D = 5.7 $\cdot 10^{-6}$ $cm^2 s^{-1}$ and D = 7.6 $\cdot 10^{-6}$ $cm^2 s^{-1}$ by Chakraborty *et al.* and Vetter *et al.*, respectively.[85,86]. These authors both employ cyclic voltammetric methods, which are fundamentally different from the techniques utilised here, making it difficult to pinpoint the source of this disagreement. Their reported diffusion coefficient differ by about 33%, proving that estimating diffusion coefficients accurately, remains challenging. Future attempts at validating this method are encouraged to study the diffusion of various electrolytes, such as HCl, NaOH and NaCl, allowing for direct comparison with the reported values by Häusler *et al.*,[33] who employed microfluidic devices and a 2D numerical description of the diffusion process as well, as described by equation 2.20. They found good agreement with values presented by Cussler.[27]

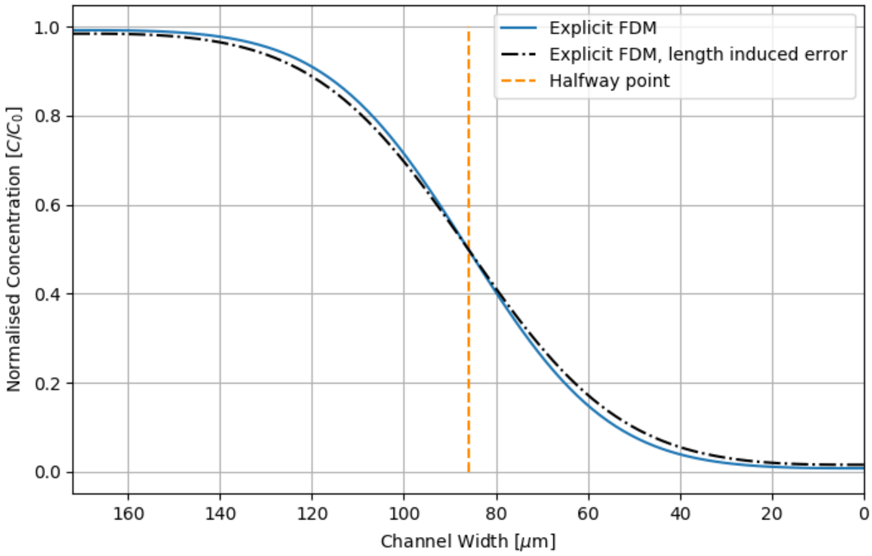

Figure 4.11: Numerically computed concentration profile at the outlets of a microfluidic channel with dimensions H/W = 100/172μm, L = 12.5mm. The flow rate Q at each inlet is 20 $\mu L\ min^{-1}$ and the diffusion coefficient D_{AB} = 13.5$\cdot 10^{-6} cm^2\ s^{-1}$

4.5. Experimental results for gallium-68 in zinc nitrate solutions

The solutions investigated were aqueous solutions of zinc nitrate with a concentration range of 1-4 M, diluted in an aqueous solution of nitric acid, in a concentration range of 0.01-1 M. 10 uL of ^{68}Ga in the form of free Ga^{3+} ions, prepared with a ^{68}Ge/^{68}Ga generator and eluted in 0.1 M HCl, was added to the aqueous solutions. These experiments performed with ^{68}Ga could not be visually inspected, due to the aqueous solutions of zinc nitrate, including the solutions containing ^{68}Ga, were fully transparent. The average flow rates were once again passively measured by assessing the weight of fluid collected in the sample vials. Results with flow rate deviations larger than 5% of the set flow rate have been discarded. After collection of the samples, 100 μL of sample was pipetted and placed in Eppendorf vials, to account for any small deviations in volume collected, and for any possible cross-contamination sources when performing the experiments. This also ensured equal measurement geometries when measuring the activities of ^{68}Ga with the automated gamma counter.

All results presented in table 4.3 were obtained with microchannel #1 (fig. 3.2a). All reported concentration fractions have been calculated according to equation 4.1. The estimated diffusion coefficients of table 4.3 have been summarised in fig. 4.12.

Small deviations in the diffusion coefficients for equal zinc nitrate concentrations, but for varying nitric acid concentrations were observed. Some Ga^{3+} ions form gallium hydroxides at low concentrations of nitric acid, with fractions ranging from 7.4% at 1 M zinc nitrate dissolved in 0.01 M nitric acid, to 22.4% at 4 M zinc nitrate dissolved in 0.01 M nitric acid. This fractions were all quantified by the program Chemical Equilibrium in Aquatic System (CHEAQS).[101] This possibly influences the overall average diffusivity of gallium atoms in their solutions, but these deviations are probably overshadowed by experimental deviations, as readily observed with the methylene blue experiments. To further map the influence of low nitric acid concentrations on the diffusivity, more experiments have to be performed. The diffusion coefficients estimated show a general trend of decreasing for an increase in zinc nitrate concentrations, as seen in fig. 4.12, except for the diffusion coefficient found for the solvent consisting of 4 M zinc nitrate dissolved in 0.01 M nitric acid. The discrepancy is of similar proportions to the deviation found in methylene blue experiment #1, as presented in table 4.2, hinting at another case of simultaneous leakage of equal magnitude. To further explore this particular possible source of error, performing microfluidic diffusion experiments with different colored dyes in aqueous solutions for each inlet is proposed. By analysing the solutions collected at each outlet for possible contaminations, should give an indication whether microfluidic systems are prone to such errors.

To quantitatively analyse the results, the viscosities for the aqueous solutions for concentrations of zinc nitrate between 1 and 4 M and a fixed concentration of 0.1 M nitric acid have been measured, with a capillary viscometer. The results are presented in fig. 4.13a. When plotting the inverse of the

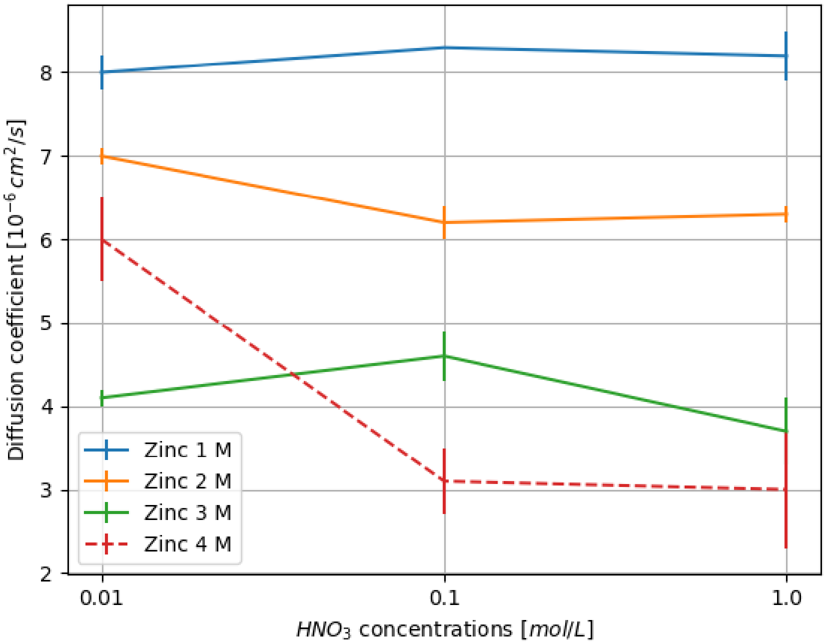

Figure 4.12: Diffusion coefficients of ^{68}Ga in solutions of zinc nitrate, ranging from concentrations of 1 to 4 M, dissolved in aqueous solutions of nitric acid, with concentrations ranging from 0.01 M to 1 M.

measured viscosity against the estimated diffusion coefficients, a generally linear relationship is observed, as seen in fig. 4.13b. The viscosities have not been directly applied to the empirical correlation relations as described in section 2.6.1, as the Stokes-Einstein model generally assumes the size of the solute to be large with respect to the solvent,[80] and for the Wilke-Chang and Siddiqi-Lucas equations, the molar volumes of zinc nitrate solutions dissolved in various concentrations of nitric acid, at their boiling point, are generally unavailable. The experimental errors in estimating the diffusion coefficient as discussed earlier probably prevent the relationship as presented in fig. 4.13b to be approximately linear. This trend holds well with the Stokes-Einstein equation,[28] and the empirical correlation relations derived from it, as they all relate the diffusion coefficient to be proportional to the inverse of the viscosity.[39,40]

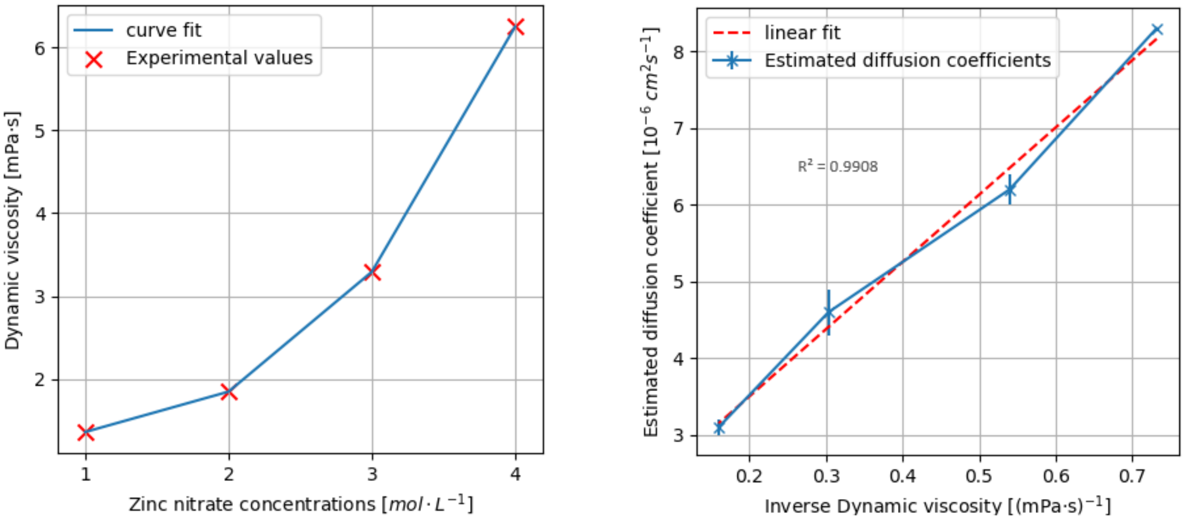

(a) Viscosities of different concentrations of zinc nitrate solutions, dissolved in an aqueous solution of a fixed concentration of 0.1 M nitric acid.

(b) Inverse viscosity plotted vs. the estimated diffusion coefficients for ^{68}Ga in various concentrations of zinc nitrate dissolved in 0.1 M nitric acid.

Figure 4.13: Viscosity measurements performed to quantitatively analyse the obtained values for the diffusion coefficients.

Table 4.3: Diffusion coefficients of ^{68}Ga in various aqueous zinc nitrate solutions, along with all experimental parameters required to estimate the diffusion coefficient.

Solution	Q_{total} $[\mu L\ min^{-1}]$	**Outlet of micro-channel**	**Fraction of total counts (mean + sem) [n=1-3]**	**Loss of activity (mean) [n=1-3]**	**Estimated D** $[10^{-6}\ cm^2\ s^{-1}]$
1 M Zn nitrate 0.01 M HNO_3	26	Upper	85.36 ± 0.30 %	16%	8.0 ± 0.2
		Lower	14.64 ± 0.30 %		
1 M Zn nitrate 0.1 M HNO_3	26	Upper	85.00 %	5.9%	8.3
		Lower	15.00 %		
1 M Zn nitrate 1 M HNO_3	26	Upper	85.10 ± 0.37 %	3.6%	8.1 ± 0.4
		Lower	14.90 ± 0.37 %		
2 M Zn nitrate 0.01 M HNO_3	26	Upper	86.51 ± 0.11 %	2.7%	7.0 ± 0.1
		Lower	13.49 ± 0.11 %		
2 M Zn nitrate 0.1 M HNO_3	26	Upper	87.50 ± 0.26 %	5.0%	6.2 ± 0.2
		Lower	12.50 ± 0.26 %		
2 M Zn nitrate 1 M HNO_3	26	Upper	87.41 ± 0.09 %	12%	6.3 ± 0.1
		Lower	12.59 ± 0.09 %		
3 M Zn nitrate 0.01 M HNO_3	26	Upper	90.17 ± 0.11 %	4.0%	4.1 ± 0.1
		Lower	9.83 ± 0.11 %		
3 M Zn nitrate 0.1 M HNO_3	26	Upper	89.47 ± 0.31 %	11%	4.6 ± 0.6
		Lower	10.53 ± 0.31 %		
3 M Zn nitrate 1 M HNO_3	26	Upper	90.76 ± 0.60 %	12%	3.7 ± 0.4
		Lower	9.23 ± 0.60 %		
4 M Zn nitrate 0.01 M HNO_3	20	Upper	85.61 ± 0.75 %	5.5%	6.0 ± 0.5
		Lower	14.39 ± 0.75 %		
4 M Zn nitrate 0.1 M HNO_3	20	Upper	90.29 ± 0.65 %	1.4%	3.1 ± 0.4
		Lower	9.71 ± 0.65 %		
4 M Zn nitrate 1 M HNO_3	20	Upper	90.30 ± 1.21 %	4.4%	3.1 ± 0.7
		Lower	9.70 ± 1.21 %		

5

Conclusion & recommendations

This study presented some production methods of ^{68}Ga in liquid targets, specifically zinc nitrate. The post-irradiation purification of ^{68}Ga is mostly achieved with ion-exchange columns, which remains fundamentally hindered by being able to perform high-purity elutions once every four hours. New purification methods in the shape of microfluidic devices are emerging as a relevant alternative. A theoretical description of the extraction of ^{68}Ga in such devices is being developed, including the diffusion of gallium isotopes in their target solution. The goal of this research was to develop a method to determine said coefficients using microfluidic devices, establishing its accuracy by benchmarking the method with solutes of known diffusivities from literature.
The developed method exploits microfluidic devices for their deeply laminar flow properties, ensuring spanwise mass transfer is dominated by diffusion. This physical process is described in a 2D numerical model, describing the fluid flow and mass transfer separately. A careful consideration of suitable methods for such descriptions have been made, with the lattice Boltzmann methods for fluid flow, and finite difference methods for mass transfer to be deemed most suitable. This model yields the diffused fraction of the initial concentration of any solute as a function of the microfluidic channel geometry, flow rate and diffusion coefficient, which can subsequently be compared with experimental results.

Benchmarking has been performed with methylthioninium chloride, more commonly known as methylene blue, which has a reported diffusion coefficient between 4.6 $\cdot$ $10^{-6} cm^2 s^{-1}$ and 7.6 $\cdot$ $10^{-6} cm^2 s^{-1}$. Preliminary numerical results fully agreed with the literature, but diffusion coefficient estimation yields discrepancies. Estimated diffusion coefficients with this method yielded an average value of 12.0 $\pm$ 1.0 $\cdot 10^{-6} cm^2 s^{-1}$, obtained with microfluidic devices of varying geometries, and with different flow rates and setups. The exact reason for this discrepancy has not been identified, but small errors presented in the results by Miložič *et al.* leaves some doubt to the validity of their results. The reported diffusion coefficients of 5.7 $\cdot$ $10^{-6} cm^2 s^{-1}$ and 7.6 $\cdot$ $10^{-6} cm^2 s^{-1}$ were obtained employing cyclic voltammetric methods, which are fundamentally different, and thus difficult to compare. Simultaneous leakage of from both co-flowing streams has been suggested as a possible source of error when operating the microfluidic device with the triangular cross-section, but further research to explore this cause of discrepancies is needed. Relative consistency in the found diffusion coefficients for methylene blue in aqueous solution for various geometries, flow rates and setups strengthen the claim of the presented diffusion coefficient. Further research into the validity of the proposed methods is required to arrive at a quantitative conclusion.
This setup is quite prone to experimental errors, as small deviations in concentration measurements can have a great impact on the resulting diffusion coefficient. As such, detection methods for the concentration of the solute with great accuracy is required, as well as high-pressure syringe pump when operating high viscosity fluids in microfluidic channels, to ensure equal flows at the outlets of the device.
Diffusion coefficient of ^{68}Ga in target solutions of several compositions were investigated. The effects of concentration of nitric acid were minimal for aqueous solutions of zinc nitrate with concentrations between 1-4 mol/L. An inverse correlation between the diffusion coefficient and the viscosity of the zinc nitrate solution was found, in accordance with empirical correlation relations.

5.1. Recommendations

5.1.1. Numerical recommendations

For the theoretical description of single-phase mass transfer in microfluidic systems, the assumption of developed flow is strongly suggested, as this should drastically cut down on computational effort required. When extending the model to solvent extraction of desired radiopharmaceuticals, kinetic-based fluid descriptions are recommended. The simplicity of the developed single phase mass transfer model makes it a very accessible method for estimating diffusion coefficients quickly.

It is further recommended to map any possible simplified relations between channel geometry, flow rates and diffusion coefficients on the computed outlet concentrations. This allows for experimental design optimisation and provides insight in how to adjust experimental parameters to obtain accurate results.

5.1.2. Experimental recommendations

To improve upon this research the obvious choice is to perform experiments with substances of which diffusivity has been studied extensively. Attractive alternatives are various electrolytes in aqueous solutions of infinite dilution as presented by Häusler *et al* and Cussler *et al.*[27,33] This should confirm the possible effectiveness of microfluidic devices as tool for determining diffusion coefficients, and provide conclusive evidence of the experimentally obtained diffusion coefficients for both methylene blue in ultrapure water and ^{68}Ga in various aqueous solution of zinc nitrate.

Upon performing similar experiments special care must be takes on selecting fluid propulsion methods, as being able to operate microfluidic devices under consistent and stable conditions greatly increases experimental swiftness.

The same holds true for equipment for accurately detecting concentration levels of the solute at the outlets of the microchannel, as small inaccuracies in concentrations can lead to large inaccuracies in diffusion coefficient estimation. Future research could study the effects of simultaneous leakage of co-flowing streams in a microfluidic device, by propulsing aqueous solutions of distinctive dyes through each inlet, and measure any possible cross-contaminations at the outlet, possibly uncovering a source of error presented in this study.

Furthermore, it would be interesting to see under which limitations microfluidic devices continue to be suitable for estimating diffusion coefficients.

Bibliography

[1] H. A. Williams et al. “A comparison of PET imaging characteristics of various copper radioisotopes”. In: *Eur J Nucl Med Mol Imaging* 32 (2005), pp. 1473–1480.

[2] C. S. Cutler et al. “Radiometals for Combined Imaging and Therapy”. In: (2012).

[3] H. O. Anger and A. Gottschalk. “Localization of brain tumors with the positron scintillation camera”. In: *Journal of Nuclear Medicine (US)* 4 (1963).

[4] S. R. Banerjee and M. G. Pomper. “Clinical applications of Gallium-68”. In: *Applied Radiation and Isotopes* 76 (2013), pp. 2–13.

[5] A. Al-Nahhas et al. “Gallium-68 PET: A New Frontier in Receptor Cancer Imaging”. In: *Anticancer Research* 27 (2007).

[6] M. Vorster et al. “Gallium-68: A systematic review of its nononcological applications”. In: *Nuclear Medicine Communications* 34 (2013), pp. 834–854.

[7] M. W. Greene and W. D. Tucker. “An improved gallium-68 cow”. In: *Intern. J. Appl. Radiation and Isotopes* 12 (1961).

[8] K. P. Zhernosekov et al. “Processing of generator-produced 68Ga for medical application”. In: *Journal of Nuclear Medicine* 48 (2007), pp. 1741–1748.

[9] F. Roesch. “Maturation of a key resource–the germanium-68/gallium-68 generator: development and new insights”. In: *Current Radiopharmaceuticals* 5 (2012), pp. 202–211.

[10] K. Kumar. “The current status of the production and supply of Gallium-68”. In: *Cancer biotherapy & radiopharmaceuticals* 35 (2020), pp. 163–166.

[11] M. K. Pandey et al. “Cyclotron production of 68 Ga via the 68 Zn(p,n) 68 Ga reaction in aqueous solution”. In: *Am J Nucl Med Mol Imaging* 4 (2014), pp. 303–310.

[12] F. Alves et al. “Cyclotron production of Ga-68 for human use from liquid targets: From theory to practice”. In: vol. 1845. 2017.

[13] N. Oehlke E.and Lengkeek et al. “Influence of metal ions on the 68Ga-labeling of DOTATATE”. In: *Applied Radiation and Isotopes* 82 (2013), pp. 232–238.

[14] N. A. Smith, D. L. Bowers, and D. A. Ehst. “The production, separation, and use of 67Cu for radioimmunotherapy: a review.” In: *Applied radiation and isotopes : including data, instrumentation and methods for use in agriculture, industry and medicine.* 70.10 (2012), pp. 2377–2383.

[15] D. Ciceri and J. M. Perera. “The use of microfluidic devices in solvent extraction.” In: *Journal of Chemical Technology and Biotechnology* 89.6 (2014), pp. 771–786.

[16] A. B. de Haan, H. B. Eral, and B. Schuur. *Industrial Separation Processes*. 2nd ed. 2020.

[17] J. D. Seader, E. J. Henley, and D. K.Roper. *Separation Process Principles: Chemical and Biochemical Operations*. 3rd ed. John Wiley & Sons, Inc, 2011.

[18] W. D. Seider et al. *Product and Process Design Principles: Synthesis, Analysis, and Evaluation*. 3rd ed. 2010.

[19] D. C. Harris. *Quantitative Chemical Analysis*. 9th ed. 2016.

[20] J. R. Backhurst, J. H. Harker, and J. F. Richardson. *Solutions to the Problems in Chemical Engineering*. Vol. 3. 2002.

[21] Carl. Hanson. “Recent advances in liquid-liquid extraction”. In: (2013).

[22] M. N. Kashid, Y. M. Harshe, and D. W. Agar. “Liquid- liquid slug flow in a capillary: an alternative to suspended drop or film contactors”. In: *Industrial & Engineering Chemistry Research* 46 (2007), pp. 8420–8430.

[23] P. A. Schweitzer. *Handbook of separation techniques for chemical engineers*. 1979.

[24] M. Rohde et al. "Fast and Efficient Purification of Medical Isotopes by Microfluidic Extraction." In: *tech. rep.* (2018).

[25] S. Goyal et al. "Thiolene and SIFEL-based microfluidic platforms for liquid-liquid extraction." In: *Sens Actuators B Chem* 190 (2014), pp. 634–644.

[26] F. Cecconi et al. "Brownian motion and diffusion: From stochastic processes to chaos and beyond". In: *Chaos: An Interdisciplinary Journal of Nonlinear Science* 15 (2005).

[27] E. L. Cussler. *Diffusion: mass transfer in fluid systems*. 2009.

[28] F. Reif. *Fundamentals of statistical and thermal physics*. 2009.

[29] R. L. Robinson et al. "Calculation of Diffusion Coefficients from Diaphragm Cell Diffusion Data". In: ().

[30] A. Alizadeh, C. A. Nieto De Castro, and W. A. Wakeham. "The Theory of the Taylor Dispersion Technique for Liquid Diffusivity Measurements". In: *International Journal of Thermophysics* 1 (1980).

[31] J. Stetefeld, S. A. McKenna, and T. R. Patel. "Dynamic light scattering: a practical guide and applications in biomedical sciences". In: *Biophysical reviews* 8 (2016), pp. 409–427.

[32] L. Yu et al. "A Comprehensive Review of Fluorescence Correlation Spectroscopy". In: *Frontiers in Physics* 9 (2021), p. 110.

[33] E. Häusler et al. "Microfluidic diffusion measurements: The optimal H-cell". In: *Chemical Engineering Science* 72 (2012), pp. 45–50.

[34] N. Miložič et al. "Evaluation of Diffusion Coefficient Determination using a Microfluidic Device". In: *Chem. Biochem. Eng* 28 (2014), pp. 213–223.

[35] C. T. Culbertson, S. C. Jacobson, and J. M. Ramsey. "Diffusion coefficient measurements in microfluidic devices". In: *Talanta* 56 (2001), pp. 365–373.

[36] K. Miyamoto et al. "Chemical imaging of the concentration profile of ion diffusion in a microfluidic channel". In: *Sens Actuators B Chem* 189 (2012), pp. 240–245.

[37] Y. Lina et al. "Measurement of temperature-dependent diffusion coefficients using a confocal Raman microscope with microfluidic chips considering laser-induced heating effect". In: *Analytica Chimica Acta* 667 (2010), pp. 103–112.

[38] Y. Lin et al. "Measurement of temperature-dependent diffusion coefficients using a confocal Raman microscope with microfluidic chips considering laser-induced heating effect". In: *Analytica Chimica Acta* 667.1-2 (2010), pp. 103–112.

[39] C. R. Wilke and P. Chang. "Correlation of diffusion coefficients in dilute solutions". In: *American Institute of Chemical Engineers journal* 1 (1955), pp. 264–270.

[40] M. A. Siddiqi and K. Lucas. "Correlations for prediction of diffusion in liquids". In: *The Canadian Journal of Chemical Engineering* 64 (1986), pp. 839–843.

[41] D. Mankoff. *Why Nuclear Imaging and Radiotherapy?* 2019, pp. 3–10.

[42] T. Kostelnik and C. Orvig. "Radioactive Main Group and Rare Earth Metals for Imaging and Therapy". In: *Chem. Rev.* 119 (2019), pp. 902–956.

[43] S. J. C. do Carmo, Peter J. H. Scott, and F. Alves. "Production of radiometals in liquid targets". In: *Radiopharmacy and Chemistry* 5 (2020).

[44] V. H. Alves et al. "Automated Purification of Radiometals Produced by Liquid Targets". In: ().

[45] J. Notni and H. J. Wester. "Re-thinking the role of radiometal isotopes: Towards a future concept for theranostic radiopharmaceuticals". In: *Journal of Labelled Compounds and Radiopharmaceuticals* 61 (2018), pp. 141–153.

[46] J.K. Shultis and R.E. Faw. *Fundamentals of Nuclear Science and Engineering*.

[47] R. A. Ferrell. "Theory of Positron Annihilation in Solids". In: *Rev. Mod. Phys.* 28 (3 1956), pp. 308–337.

[48] G. Choppin et al. *Radiochemistry and Nuclear Chemistry: Fourth Edition*. 2013, pp. 1–858.

[49] *Gallium-68 Cyclotron Production*. TECDOC Series 1863. 2019.

[50] M.Jensen and J. Clark. “Direct production of Ga-68 from proton bombardment of concentrated aqueous solutions of [Zn-68] Zinc Chloride”. In: 2011, pp. 288–292.

[51] F. Alves et al. “Production of copper-64 and gallium-68 with a medical cyclotron using liquid targets”. In: *Modern Physics Letters A* 32 (2017).

[52] G. M. Dias et al. “Peptide radiolabeling and in vivo imaging using Ga-68 directly produced in liquid targets”. In: *Journal of Labelled Compounds & Radiopharmaceuticals*. Vol. 60. 2017, S400–S400.

[53] E. Oehlke et al. “Production of Y-86 and other radiometals for research purposes using a solution target system”. In: *Nuclear Medicine and Biology* 42 (2015), pp. 842–849.

[54] J. N. Reddy. *Principles of Continuum Mechanics: An Introduction for Engineers*. 2017.

[55] G. K. Batchelor. *An Introduction to Fluid Dynamics*. 2000.

[56] B. W. Rowe. *Basic Flow Theory*. 2012, pp. 25–48.

[57] S. N. Aristov, D. V. Knyazev, and A. D. Polyanin. “Exact solutions of the Navier-Stokes equations with the linear dependence of velocity components on two space variables”. In: *Theoretical Foundations of Chemical Engineering* 43 (2009), pp. 642–662.

[58] G. M. Whitesides. “The origins and the future of microfluidics”. In: *Nature* 442 (2006), pp. 368–373.

[59] T. M. Squires and S. R. Quake. “Microfluidics: Fluid physics at the nanoliter scale”. In: *Reviews of modern physics* 77 (2005), pp. 980–981.

[60] J. G. Kralj, H. R. Sahoo, and K. F. Jensen. “Integrated continuous microfluidic liquid-liquid extraction”. In: ().

[61] M. R. Lewis et al. “Production and purification of gallium-66 for preparation of tumor-targeting radiopharmaceuticals”. In: *Nuclear Medicine and Biology* 29 (2002), pp. 701–706.

[62] J. D. Anderson and J. Wendt. *Computational fluid dynamics*. Vol. 206. 1995.

[63] J. H. Ferziger, M. Perić, and R. L. Street. *Computational methods for fluid dynamics*. Vol. 3. 2002.

[64] R. Bhaskaran and L. Collins. “Introduction to CFD basics”. In: *Cornell University-Sibley School of Mechanical and Aerospace Engineering* (2002), pp. 1–21.

[65] H. K. Versteeg and W. Malalasekera. *An introduction to computational fluid dynamics: the finite volume method*. 2007.

[66] G. R. McNamara and G. Zanetti. “Use of the Boltzmann equation to simulate lattice-gas automata”. In: *Physical review letters* 61 (1988), p. 2332.

[67] S. Chen and G. D. Doolen. “Lattice Boltzmann method for fluid flows”. In: *Annual review of fluid mechanics* 30 (1998), pp. 329–364.

[68] H. Huang, M. C. Sukop, and X. Lu. *Multiphase Lattice Boltzmann Methods: Theory and Application*. 2015.

[69] J. Clerk Maxwell. “On the dynamical theory of gases”. In: *Philosophical Transactions of the Royal Society* 157 (1867), pp. 44–89.

[70] L. P. Kadanoff. “On Two levels”. In: *Physics Today* 39 (1986), pp. 7–9.

[71] T. Krüger et al. *The Lattice Boltzmann Method: Principles and Practice*. 1st ed. 2017.

[72] P. L. Bhatnagar, E. P. Gross, and M. Krook. “A Model for Collision Processes in Gases. I. Small Amplitude Processes in Charged and Neutral One-Component Systems”. In: *Phys. Rev.* 94 (3 1954), pp. 511–525.

[73] M. C. Sukop and D. T. Thorne. *Lattice Boltzmann Modeling*. 2006.

[74] S. Chapman and T. G. Cowling. *The mathematical theory of non-uniform gases: an account of the kinetic theory of viscosity, thermal conduction and diffusion in gases*. 1990.

[75] W. M. Deen. *Analysis of transport phenomena*. Vol. 2. 1998.

[76] D. Kuzmin. *A guide to numerical methods for transport equations*. 2010.

[77] K. Hanjalic et al. *Analysis and modelling of physical transport phenomena*. 2007.

[78] S. Mazumder. *Numerical methods for partial differential equations: finite difference and finite volume methods*. 2015, pp. 51–58.

[79] W. F. Ames. *Numerical methods for partial differential equations*. 2014.

[80] J. T. Edward. “Molecular volumes and the Stokes-Einstein equation”. In: *Journal of chemical education* 47 (1970), p. 261.

[81] J. Li and P. W. Carr. “Accuracy of empirical correlations for estimating diffusion coefficients in aqueous organic mixtures”. In: *Analytical chemistry* 69 (1997), pp. 2530–2536.

[82] R. H. Perry and D. W. Green. “Perry’s chemical engineers’”. In: *Handbook–seventh Edition–Sections* (2008).

[83] F. Rouessac and A. Rouessac. *Chemical Analysis Modern Instrumentation Methods and Techniques Second Edition*. 2nd.

[84] H.-H. Perkampus. *UV-VIS Spectroscopy and Its Applications*. 1992.

[85] A. Chakraborty, S. Ahmed, and S. K. Saha. “Electrochemical Studies of Progressively Alkylated Thiazine Dyes on a Glassy Carbon Electrode (GCE) in Water, Ethanol, and Triton X-100 Media †”. In: ().

[86] K. Vetter and J. Bardeleben. “Überspannung und Gleichgewichtspotentiale der Methylenblau/ Leukomethylenblau–Redoxelektrode”. In: *Zeitschrift für Elektrochemie, Berichte der Bunsengesellschaft für physikalische Chemie* 61 (1957), pp. 135–141.

[87] A. J. C. Ladd. “Numerical simulations of particulate suspensions via a discretized Boltzmann equation. Part 1. Theoretical foundation”. In: *Journal of fluid mechanics* 271 (1994), pp. 285–309.

[88] A. J. C. Ladd and R. Verberg. “Lattice-Boltzmann simulations of particle-fluid suspensions”. In: *Journal of statistical physics* 104 (2001), pp. 1191–1251.

[89] Q. Lou, Z. Guo, and B. Shi. “Evaluation of outflow boundary conditions for two-phase lattice Boltzmann equation”. In: *Physical Review E - Statistical, Nonlinear, and Soft Matter Physics* 87 (2013).

[90] I. Ginzbourg and P. M. Adler. “Boundary flow condition analysis for the three-dimensional lattice Boltzmann model”. In: *Journal de Physique II* 4 (1994), pp. 191–214.

[91] I. Ginzburg and D. d’Humieres. “Multireflection boundary conditions for lattice Boltzmann models”. In: *Physical Review E* 68 (2003).

[92] C. E. Brennen. “An internet book on fluid dynamics”. In: *Index for Internet Book on Fluid Dynamics* (2006).

[93] M. Junk and Z. Yang. “Outflow boundary conditions for the lattice Boltzmann method”. In: *Progress in Computational Fluid Dynamics, an International Journal* 8 (2008), pp. 38–48.

[94] N. Dombrowski et al. “The influence of Reynolds number on the entry length and pressure drop for laminar pipe flow”. In: *The Canadian Journal of Chemical Engineering* 71 (1993), pp. 472–476.

[95] D. Melgoza, A. Hernández-Ramírez, and J. M. Peralta-Hernández. “Comparative efficiencies of the decolourisation of Methylene Blue using Fenton’s and photo-Fenton’s reactions”. In: *Photochemical and Photobiological Sciences* 8 (2009), pp. 596–599.

[96] A. Fernandez-Perez and G. Marban. “Visible Light Spectroscopic Analysis of Methylene Blue in Water; What Comes after Dimer?” In: *ACS omega* 5 (2020), pp. 29801–29815.

[97] J. Yao and C. Wang. “Decolorization of Methylene Blue with TiO 2 Sol via UV Irradiation Photocatalytic Degradation”. In: *International Journal of Photoenergy* 2010 (2010).

[98] F. Pires et al. “Methylene Blue A Trendy Photosensitizer in Medicine and in Solar-Energy Conversion Systems”. In: ().

[99] A. Fernández-Pérez and G. Marbán. “Visible Light Spectroscopic Analysis of Methylene Blue in Water”. In: *Journal of Applied Spectroscopy* (2022), pp. 1–7.

[100] D. F. Othmer. *Kirk-Othmer encyclopedia of chemical technology*. 2004.

[101] W. Verweij. “CHEAQS, a program for calculating CHemical Equilibria in AQuatic Systems”. In: *National Institute for Public Health and the Environment* (1999).